JQS **Journal of Quaternary Science** **QRA**
Quaternary Research Association

A 600-year marine record associated with the dynamics of the eastern Penny Ice Cap (Baffin Island, Nunavut, Canada)

MARÍA-EMILIA RODRÍGUEZ-CUICAS,[1]* JEAN-CARLOS MONTERO-SERRANO,[1] GUILLAUME ST-ONGE[1,2] and ALEXANDRE NORMANDEAU[3]
[1]Institut des sciences de la mer de Rimouski, Québec-Océan and GEOTOP, Université du Québec à Rimouski, Rimouski, QC, Canada
[2]Canada Research Chair in Marine Geology, Rimouski, QC, Canada
[3]Geological Survey of Canada (Atlantic), Natural Resources Canada, Dartmouth, NS, Canada

ABSTRACT: Two composite sedimentary sequences sampled in the ice-proximal (12CS) and ice-distal (02CS) areas of Coronation Fjord (Baffin Island, Nunavut, Canada) were investigated in order to reconstruct the effect of climate variability on 600 years of changes in sediment transfer from the eastern Penny Ice Cap (PIC). Detrital proxies, and physical and sedimentological analyses revealed that glacial meltwater discharges led to frequent rapidly deposited layers (RDLs) in ice-proximal settings. RDLs in ice-distal settings involved the sudden release of a large quantity of sediment-laden water during floods probably originating from adjacent fjords with large sandur deltas. Laminated sediments with ice-rafted debris throughout the Little Ice Age interval in the ice-proximal environment suggest that colder conditions promoted glacier growth, leading to successive episodes of turbid hyperpycnal meltwater plumes and iceberg calving in Coronation Fjord. Since 1850 CE, the accelerated Coronation retreat in response to modern warming has led to increased sedimentation rates, abrupt mineralogical and grain size proxy variations and more frequent RDLs. Similar trends between the detrital proxies of the ice-proximal core and Atlantic Multidecadal Oscillation record and Arctic surface air temperature suggest high connectivity between atmospheric and sea surface temperature variations and PIC dynamics over the last 600 years.
© 2023 The Authors. *Journal of Quaternary Science* Published by John Wiley & Sons Ltd.

KEYWORDS: Baffin Island; geochemistry; glacier dynamics; mineralogy; Penny Ice Cap; rapidly deposited layers; sediment dynamics; sedimentology

Introduction

The Canadian Arctic Archipelago (CAA) has suffered one of the largest glacier volume losses in the past decade, making this region one of the largest contributors to global sea level rise (Radić & Hock, 2010; Gardner et al., 2011; Harig & Simons, 2016; Noël et al., 2018; Ciracì et al., 2020). Lenaerts et al. (2013) estimated that the CAA glacier mass loss by the end of the 21st century will contribute ~0.35 ± 0.24 mm a^{-1} to global sea level rise. Approximately 22% of glacier ice in the CAA is contained on Baffin Island (mainly in the Penny and Barnes Ice Caps) and is considered the last vestiges of the Laurentide Ice Sheet (Zdanowicz et al., 2012; Fig. 1). Glaciers and ice caps on Baffin Island have lost ~23.8 Gt a^{-1} of ice, which has contributed to a rise of 0.07 mm a^{-1} in global sea level during recent decades (Gardner et al., 2012; Van Wychen et al., 2015; Schaffer et al., 2017).

Penny Ice Cap (PIC) on the Cumberland Peninsula has a total area of 6410 km^2 and is the most southerly part of the CAA, which makes it highly sensitive to climate change (Zdanowicz et al., 2012). Instrumental data have shown that the velocity of the tidal glaciers of the PIC decelerated from 53 to 32 m a^{-1} between 1985 and 2011 (Van Wychen et al., 2015; Schaffer et al., 2017), and the greatest iceberg discharge contribution occurred from Coronation Glacier (Coronation Fjord) at rates of

8–12 Mt a^{-1} (Van Wychen et al., 2015). However, studies of glacier dynamics in the CAA have not resolved whether the observed variations are unprecedented over the last few thousand years (Oerlemans, 2005; Schaffer et al., 2017).

Although records of Holocene paleoclimatic conditions on Baffin Island exist (ice cores: Fisher et al., 1998; Zdanowicz et al., 2012; remote sensing: Van Wychen et al., 2015; Schaffer et al., 2017; lacustrine sediments: Briner et al., 2006; Thomas & Briner, 2009; Briner et al., 2009; Thomas, et al., 2011; Narancic et al., 2021), detailed reconstructions of past environmental changes in sediment records of fjords are less abundant (e.g. Syvitski & Schafer, 1985; Syvitski, 1989; Syvitski et al., 2022). Fjords represent transitions from the terrestrial to the marine environment for most glaciers that drain ice caps. Similarly, geomorphological features and high sedimentation rates have the potential to make fjords ideal depositional environments to preserve records of climate and environmental changes with high temporal resolution (Syvitski, 1989; Howe et al., 2010; Syvitski et al., 2022). In addition, the sedimentary dynamics of glaciers and ice sheets can generate considerable temporal and spatial variability in glaciogenic depositional processes (e.g. Dowdeswell et al., 2015). Indeed, a variety of sedimentary processes in glacial environments can be linked to glacier melt processes, such as iceberg-delivered debris, glaciogenic debris flows and turbidity currents (Shaw, 1987; Syvitski, 1989; Syvitksi & Normandeau, 2023). Thus, the configuration and sedimento-logical characteristics of these deposits can be used to identify

*Correspondence: María-Emilia Rodríguez-Cuicas, as above.
E-mail: memilia.rc@gmail.com
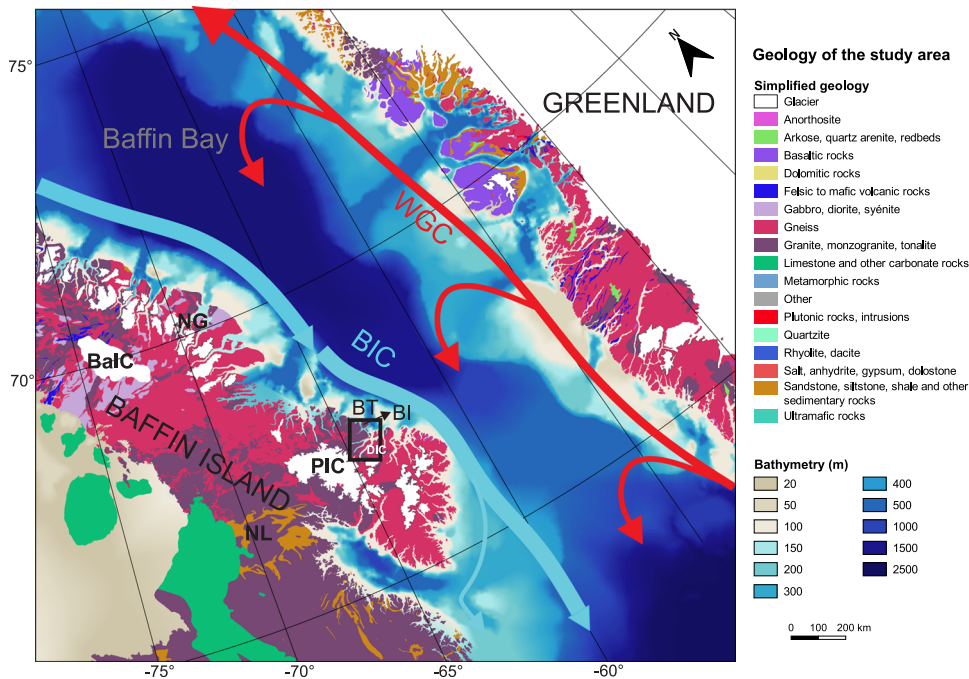
Figure 1. Regional geology and location of the Penny Ice Cap (PIC) on Baffin Island. Arrows represent the relatively warm West Greenland Current (WGC) and the cold Baffin Island Current (BIC). Abbreviations: Broughton Trough (BT), Broughton Island (BI), Barnes Ice Cap (BalC), Divide Ice Cap (DIC), Naqsaq Glacier (NG) and Nettilling Lake (NL). [Color figure can be viewed at wileyonlinelibrary.com]

periods of glacial activity (Dowdeswell et al., 2015; Jenner et al., 2018; Lévesque et al., 2020).

In this context, the present study focuses on two composite sediment cores (AMD1803-02CS and AMD2019-804-12CS) collected along Coronation Fjord in southeastern Baffin Bay (Fig. 2). These sedimentary records provide a robust overview of the temporal variation in sediment transfer from the eastern sector of the PIC beyond the instrumental record. Lead-210 (^{210}Pb), plutonium-239 and -240 ($^{239+240}$Pu), paleomagnetic and radiocarbon analyses, together with physical, sedimentological, mineralogical and elemental geochemical properties are combined in these composite sediment cores to: (i) identify the types and drivers of rapidly deposited layers (RDLs) in proximal to distal glacial environments; (ii) examine how past climate and ocean changes have influenced the frequency of RDLs observed in both proximal and distal environments; and (iii) assess the significance of recent glaciological changes in the eastern PIC. Overall, our multiproxy approach allows us to reconstruct glacier dynamics and their connection to regional climate history during the last 600 years through an understanding of the predominant sedimentary processes in Coronation Fjord.

Regional setting

Geology, physiography, climate and fjord circulation

Maktak, Coronation and North Pangnirtung fjords are situated on the Cumberland Peninsula and were carved into bedrock during early Pleistocene or even the Pliocene glaciations (Gilbert, 1982a; Syvitski & Piper, 1990). The bedrock on the eastern Cumberland Peninsula consists of Precambrian gneiss, granite–tonalite and quartz monzonite, while carbonate rocks are absent (Fig. 1; Clarke & Upton, 1971; Jackson & Berman 2000; St-Onge et al., 2009). The fjords were carved to a maximum depth to bedrock of 565 m in Maktak Fjord, 685 m in Coronation Fjord and 440 m in North Pangnirtung Fjord (Fig. 2; Syvitski et al., 2022). They served as conduits for glacial ice originating from the PIC, which discharges through the Broughton Trough into Baffin Bay (Fig. 1; Gilbert, 1982a; Schatz et al., 2013).

At the regional level, the climate of the east coast of Baffin Island was strongly modulated by patterns of ocean circulation in Baffin Bay during the Holocene (Münchow et al., 2015). This basin contains the Baffin Island Current (BIC), which flows southward in the western part of Baffin Bay and originates from cold Arctic waters, and the West Greenland Current (WGC), which flows northward along the western coast of Greenland before mixing with the BIC in Smith Sound (Fig. 1; Tang et al., 2004). The WGC is fed by Irminger Current (IC) water, becoming the northern limb of the North Atlantic subpolar gyre (Tang et al., 2004). Changes in the balance between the relatively warm and salty WGC and the outflow of cold, low-salinity surface water from the BIC directly impact both temperature and the amount of precipitation on Cumberland Peninsula.

Summers on Cumberland peninsula (June, July, August) are cool and short with a mean temperature of 4.3°C, while the other three seasons (September–May) are cold with a mean temperature of −13.1°C in 2022 (Broughton Island, Fig. 1; https://climat.meteo.gc.ca). Modern precipitation for the eastern Baffin Island coast reaches 250 ± 150 mm a^{-1} and the largest discharge events occur during early summer (Syvitski et al., 2022). During the winter period, the fjord is covered with sea ice and the modern pattern of break-up starts with open water near the ice front in June and the landfast sea ice breaks up in the outer channels in July.

Locally, circulation in the fjords and exchange of water with Baffin Bay may be restricted (Gilbert et al., 1989). These fjords are dominated by freshwater input at their heads. However, tidal currents, wave activity, the Coriolis force and side entry drainage also influence the circulation and sedimentary processes in these basins (Gilbert, 1982b; Syvitski, 1989; Schatz et al., 2013). Tidal activity in Coronation Fjord has a small range of 1.1 m (Gilbert, 1982a). However, the absence of sills within the fjord allows exchange of sea water and quasi-continuous circulation at depth (Gilbert, 1982a; Syvitski, 1989). The Coriolis force is highly influential in controlling the deposition of suspended particles, causing a noticeably higher accumulation of sediment along the southern side of the fjords compared to the north side (Gilbert, 1982a; Gilbert, 1983; Syvitski, 1989; Syvitski & Shaw, 1995). During the winter period, ice cover limits the circulation by preventing wind waves and tidal currents and producing a layer of fresh
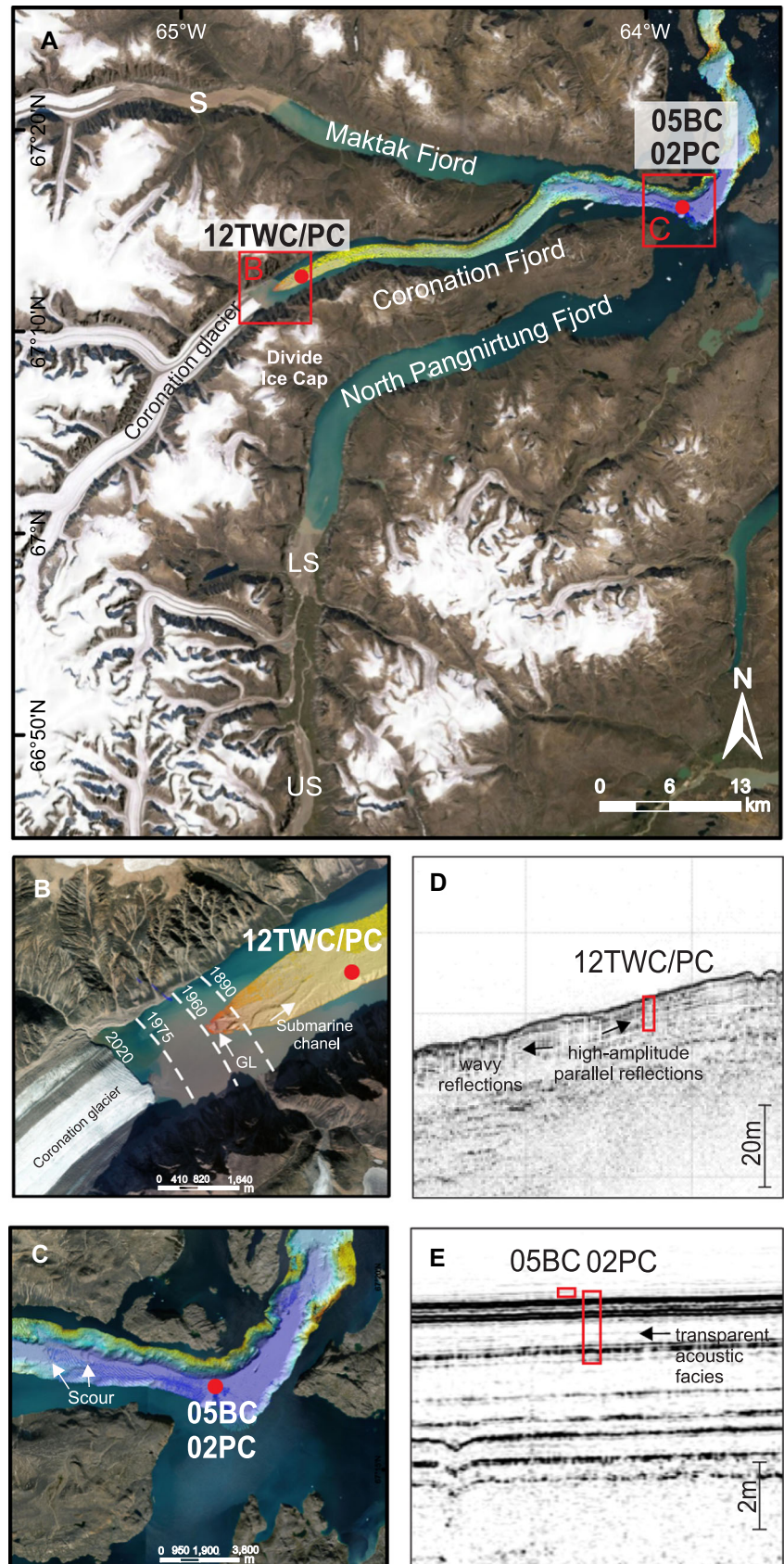
Figure 2. (A–C) MODIS satellite image from 11 May 2020 showing a snapshot of Maktak, Coronation and North Pangnirtung Fjords (source: NASA Worldview), as well as the bathymetry and the location of the cores in this study. The bathymetric data are from Normandeau et al. (2019). (B) Dashed line suggests the positions of the ice margin at 1890, 1960, 1975 and 2020 (Davis, 1985; Pendleton et al., 2017; Syvitski & Normandeau, 2023). (D–E) Sub-bottom profiles across coring stations. US, upper sandur; LS, lower sandur; GL, grounding line. [Color figure can be viewed at wileyonlinelibrary.com]

meltwater before break-up. By late winter, the growth of ice ceases and the vertical circulation may slow or stop (Gilbert, 1983).

Sedimentation

Maktak, North Pangnirtung and Coronation Fjords have been filled with glaciomarine sediments (58, 36 and 94 m thick, respectively; Gilbert, 1985). Contemporary sedimentary processes in these basins are characterized by (i) ice-rafted debris (IRD); (ii) suspension fall-out of fine-grained sediment from meltwater plumes; (iii) deposition of graded sand beds from gravity flows, such as turbidity currents and hyperpycnal flows; and (iv) eolian transport from sandy surfaces, mainly from Maktak and North Pangnirtung Fjords (Gilbert, 1982b). IRD is common in the sedimentary record within Coronation Fjord due

to the presence of outlet tidewater glaciers and calving icebergs (Gilbert, 1982b; Syvitski, 1989). Meltwater plumes are the main transport agents and suppliers of fine-grained sediments (Gilbert, 1982b; Syvitski, 1989). During periods of high meltwater discharge, gravity flows lead to sediment accumulation in zones proximal to Coronation Glacier (Gilbert, 1982b; Syvitski, 1989). A similar process also occurs on the delta slopes at the heads of Maktak and North Pangnirtung Fjords (Gilbert, 1983; Syvitski & Normandeau, 2023). Turbidity current deposits have been identified as several distinct intervals of 1–5 cm thick normally graded layers in Maktak Fjord (Schatz et al., 2013) and prodelta channels covered with cyclic steps are present at the head of Maktak Fjord (Syvitski & Norm&eau, 2023). Finally, eolian sediments are deposited relatively close to glacier margins and are typically represented by well-sorted medium-grained sand (Gilbert, 1983; McKenna-Neuman & Gilbert, 1986). Superficial seabed sediments are predominantly composed of marine grayish-brown silts and clays with high alkali feldspar (>20%), plagioclase (>20%), clay mineral (<20%), amorphous silica (~15%) and quartz (~10%) contents (Andrews et al., 2018; Andrews, 2019).

Materials and methods

Sediment cores

Sediment cores were recovered onboard the Canadian Coast Guard Ship (CCGS) icebreaker *Amundsen* along Coronation Fjord during the 2018 and 2019 ArcticNet expeditions (Table 1; Fig. 2). Cores AMD1803-05BC (box core) and AMD1803-02PC (piston core), hereafter referred to as 05BC and 02PC, were recovered at the junction of three fjords (North Pangnirtung, Coronation and Maktak). Cores AMD2019-804-12PC/TWC (piston core and companion trigger weight core), hereafter referred to as 12PC/TWC, were collected at the head of Coronation Fjord. Cores 05BC and 12TWC (first 50 cm) were evenly sampled at 1-cm intervals, whereas cores 02PC and 12PC were sampled at 3- to 4-cm intervals. Cores 02PC and 12PC/TWC were subsampled with u-channels (1.5-m-long u-shaped plastic liners with a 2 × 2-cm cross-section) for paleomagnetic analyses. Both coring sites were identified using high-resolution seismic profiles and multibeam bathymetry data (Montero-Serrano et al., 2018; Normandeau et al., 2019). Subbottom profiles were acquired using a Knudsen 3260 CHIRP sonar at a frequency of 3.5 kHz. The multibeam bathymetry data were obtained from a Kongsberg EM302 multibeam echosounder (30 kHz) operated with the Seafloor Information System (SIS). All the acquired multibeam data were postprocessed using CARIS HIPS&SIPS 11.1 software.

Laboratory analyses

Multi-sensor core logger analyses (physical and chemical properties)

All whole cores were X-radiographed using a GEOTEK X-ray computed tomography (X-CT) system. The digital X-ray images obtained by X-CT are useful to visualize different facies and sedimentary structures (St-Onge et al., 2007). Next, and prior to core splitting, wet bulk densities (determined from gamma ray attenuation) were measured at 1-cm intervals using a GEOTEK multi-sensor core logger (MSCL). The cores were then split, described and digitally photographed. The low-field volumetric magnetic susceptibilities (k_{LF}), diffuse spectral reflectance and chemical composition via portable X-ray fluorescence (pXRF) were measured using a GEOTEK MSCL system at 0.5- cm intervals for core 05BC and 1-cm intervals for cores 02PC/TWC and 12PC/TWC. Reflectance was obtained by using a hand-held Minolta CM-2600d spectrophotometer coupled to the MSCL, and the sediment color is expressed according to the L*, a* and b* color space of the International Commission of Light (e.g. St-Onge et al., 2007). Only the L* and a* indexes are used in this study. L* is a black-to-white scale (0–100), and a* is a green–red scale (-60 to $+60$) (St-Onge et al., 2007; Debret et al., 2011). The pXRF scans were made using an energy-dispersive Olympus Innov-X DELTA portable X-ray fluorescence analyzer integrated with the MSCL and equipped with a 40-kV rhodium anode X-ray tube. The pXRF analyzer was calibrated using the Olympus Innov-X standard alloy #316. pXRF analysis was conducted using GeoChem with two beams (40 and 10 kV) with a 60-s exposure time per beam.

Grain size

Sediment grain size analyses (<2-mm fraction) were performed using a Beckman Coulter LS13320 laser diffraction grain size analyzer, with a detection range of 0.04–2000 μm (at a 1 cm down-core interval in core 05BC and 3 cm interval in cores 02PC and 12PC/TWC). The sediment samples were pretreated with 10 mL hydrogen peroxide (H_2O_2; 30%, v/v) to remove the organic matter. Biogenic silica was not removed prior to grain size measurements, as it appeared to be negligible (<0.1%, as suggested by its non-detection in the bulk sediment XRD diffractograms). Likewise, carbonate was not removed from sediment samples, as this can provide information on sediment provenance (e.g. Andrews et al., 2018; Andrews, 2019). Samples were deflocculated by successive washing with distilled water and subsequently disaggregated using an in-house rotator for 12 h prior to particle size measurements. The grain size distribution and statistical parameters were calculated using GRADISTAT software version 9.1 (Blott & Pye, 2001). The grain size distributions can help to characterize lithologic changes and document changes in sediment transport regimes over time (e.g. Casse et al., 2017; Gamboa et al., 2017; Deschamps et al., 2018). Furthermore, the gravel-sized clast abundance was determined using the method described by Grobe (1987), which consists of counting the >2-mm fraction on the X-CT scan images of the core in contiguous 2-cm windows. The abundance of gravel-sized clasts is used here to identify intervals in the cores influenced by abundant ice rafting (e.g. IRD and sea ice transport; Andrews, 2000). In addition, the sortable silt mean size ($\overline{SS}$) flow speed proxy, which corresponds to the mean grain size of the non-cohesive silt fraction (10–63 μm) and the percentage of sortable silt (SS%) in the <63-μm fraction (McCave

Table 1. Location of the sampling sites, water depth and length of the cores used in this study.

Core	Latitude (°N)	Longitude (°W)	Zone	Water depth (m)	Core length (cm)
AMD1803-05BC	67.28412	−63.91034	Ice-distal	609	43
AMD1803-02PC	67.28464	−63.90958	Ice-distal	609	222
AMD2019-804-12PC/TWC	67.21934	−64.71831	Ice-proximal	189	619/277

et al., 1995) was calculated for both cores using the approach developed by McCave and Andrews (2019a).

Quantitative bulk mineralogy

Quantitative X-ray diffraction mineralogy (qXRD) of the <2-mm sediment fraction was studied according to the method developed by Eberl (2003). For this, ~1 g of each sample was spiked with 0.25 g of corundum and then ground in a McCrone micronizing mill using 5 mL of ethanol to obtain a homogenous powder. Next, 0.5 mL of Vertrel was added to the mixture to prevent the possible agglomeration of finer particles. The powder sample was then sieved (<300 μm), back-loaded into the holders and analyzed on a PANalytical X'Pert powder diffractometer. Samples were scanned from 5° to 65° two-theta in steps of 0.02° two-theta, with a counting time of 2 s per step. For the quantification of the major mineralogical components, sediment XRD scans were converted into mineral weight per cent (wt.%) using the Excel macro program ROCKJOCK v11 (Eberl, 2003). This program uses a full-pattern fitting method that permits the quantification of whole sediment mineralogy with a precision of ±3 wt.% (Eberl, 2003). The calculated total mineral wt.% was normalized to a sum of 100%. The principal minerals that were analyzed by this method were quartz (Qz), K-feldspar (Kfs), plagioclase (Pl), dolomite (Dol), amphibolite (Am), pyroxene (Px), Fe-bearing (Fe-b) minerals, smectite (Sme), illite (Ill, including muscovite), chlorite (Chl) and biotite (Bt).

Chronology

^{210}Pb and $^{239+240}Pu$ analyses

The chronology of core 05BC was assessed based on ^{210}Pb and $^{239+240}Pu$ measurements. Sediment samples from the top 25 cm of core 05BC (at 1-cm intervals) were freeze-dried, homogenized and sealed in Petri dishes for >21 days to allow secular equilibrium. Next, the measurements of radioisotope ^{210}Pb were performed at the Institut des sciences de la mer de Rimouski (ISMER) by gamma spectrometry following Reyss et al. (1995). The counting error was evaluated at 1σ ~ 5%. ^{210}Pb excess activities were calculated by subtracting the ^{226}Ra-supported activity from the total ^{210}Pb activity. A constant rate supply ^{210}Pb model was used to determine sedimentation rates and to estimate ages (Appleby & Oldfield, 1983). In addition, freeze-dried sediment samples (2 g) from the top 25 cm of core 05BC (at 1-cm intervals) were analyzed at Northern Arizona University for $^{239+240}Pu$ concentrations using a Thermo X2 quadrupole inductively coupled plasma–mass spectrometry system and following the method described in Ketterer et al. (2004). The age model from core 05BC (Supporting Information Fig. S1), including ^{210}Pb, $^{239+240}Pu$ and accelerator mass spectrometry (AMS) ^{14}C data, was developed with the 'serac' R package (Bruel & Sabatier, 2020). The results of the ^{210}Pb dating were also used to build the age model of the composite sequence that includes cores 05BC and 02PC. ^{210}Pb measurements from the top 123 cm of core 12TWC were performed at the Geotop Research Center (Montréal, Canada) by alpha spectrometry (Fig. S2). Before the analysis, all samples were sieved through a 150-μm Nitex® mesh to prevent biases in ^{210}Pb data linked to bulk grain size variations; the samples were then oven-dried (70°C), crushed and homogenized with an agate mortar.

Palaeomagnetic analysis

Paleomagnetic data were acquired at 1-cm intervals on u-channel samples using a 2 G Enterprises™ u-channel cryogenic magnetometer model 755 SRM and a pulse magnetizer for the induction of isothermal remanent magnetizations (IRMs). Due to the finite spatial resolution of the magnetometer's pickup coils, each measurement integrates a stratigraphic interval of 7–8 cm (Philippe et al., 2018) and to eliminate edge effects the data points from the upper and lower 4 cm of each u-channel were not used (Weeks et al., 1993). The natural remanent magnetization (NRM) was measured and then stepwise demagnetized by alternating field (AF) demagnetization at peak fields of 0 to 85 mT at 5-mT increments. A continuous field of 50 μT (direct current or DC bias field) and a 100-mT alternating field were then applied to the sample to impart an anhysteretic remanent magnetization (ARM). Subsequently, DC pulse fields of 300 mT (IRM) and 950 mT (saturated isothermal remanent magnetization; SIRM) were applied, and the IRM was progressively demagnetized following the same procedure used for ARM. SIRM was demagnetized at peak fields of 0, 10, 30 and 50 mT.

The magnetic inclination of the characteristic remanent magnetization (ChRM) was calculated using a least squares line fitting procedure (Kirschvink, 1980) with the Excel macro developed by Mazaud (2005). This computation also provided the maximum angular deviation (MAD) values and the median destructive field (MDF). The MAD values provide a quantitative measurement of the analytical uncertainty and an estimation of the quality of the paleomagnetic data. MAD values < 5° are indicative of high-quality directional data (Stoner & St-Onge, 2007). These analyses allow us to identify possible rapidly deposited layers such as turbidites and debrites, which are characterized by low-quality paleomagnetic data and shallow inclinations (e.g. St-Onge et al., 2004; Tanty et al., 2016; Lévesque et al., 2020; Philippe et al., 2022). Finally, the MDF of the NRM was also calculated. The MDF represents the required demagnetization field necessary to reduce the initial magnetic remanence by half of its initial intensity. The MDF reflects the mean coercivity state of the magnetic grain assemblage and depends on both the grain size and the mineralogy (e.g. Stoner & St-Onge 2007).

Radiocarbon analysis

To support the chronostratigraphical framework derived from the paleomagnetic data, we used eight AMS radiocarbon (^{14}C) ages (Table 2). Six samples (five in core 12PC and one in core 05BC) of well-preserved marine shell fragments (mainly *Portlandia arctica*) were measured, while one sample of mixed benthic foraminiferal species from core 02PC was measured (Table 2). AMS ^{14}C measurements were performed at the Keck Carbon Cycle AMS laboratory at the University of California – Irvine (California, USA) and the Alfred Wegener Institute Helmholtz Centre for Polar and Marine Research (Bremerhaven, Germany). Note that very few foraminifera (<0.02 mg) were recovered from core 02PC, which was not enough to perform AMS analysis. In the Arctic, this recoverable amount is related to the poor preservation of foraminifera and mollusks due to calcium carbonate dissolution in bottom waters (Aksu, 1983; de Vernal et al., 1992; Azetsu-Scott et al., 2010). The local marine reservoir age correction (ΔR) from AMS ^{14}C ages was calculated from paired ^{14}C and paleomagnetic dates using the online program deltar (Reimer & Reimer, 2017; http://calib.org/deltar/) based on the new Marine20 calibration curve (Heaton et al., 2020). Next, the conventional ^{14}C ages obtained in this study were calibrated using the Marine20 curve by assuming a regional reservoir age correction of ΔR = −154 ± 56 years for core 12PC and ΔR = 15 ± 169 years for core 02PC (Tables 2 and 3; Supporting Information Fig. S3). The difference between

Table 2. Accelerator mass spectrometry (AMS) radiocarbon dates and calibrations for cores 12PC, 05BC and 02PC, with different reservoir ages.

Laboratory number	Core	Material dated	Depth (cm)	^{14}C age (a BP)	Error	$\triangle R = -162 \pm 68$ Median (CE)	Range 2σ	$\triangle R = 15 \pm 169$ Median (CE)	Range 2σ
UCIAMS-233572	12PC	Shell fragment	151	440	30	1835	1730–1950		
UCIAMS-233573	12PC	Shell fragment	168	525	15	1809	1669–1950		
UCIAMS-233566	12PC	Shell fragment	238	685	15	1645	1476–1830		
UCIAMS-233568	12PC	Shell fragment	404	750	15	1586	1438–1759		
UCIAMS-233570	12PC	Shell fragment	482	900	15	1458	1317–1622		
AWI-5664.1.1	05BC	Shell fragment	14.5	103.8	0.9 pMC*			Modern (>1962 CE)*	
AWI-6309.1.1	02PC	Mixed-benthic foraminifera	39	1046	63			1489	1159–1871

*Date constrained by $^{239+240}$Pu dates (1952 and 1963 CE corresponding with the dates of atmospheric nuclear testing; Ketterer et al., 2002, 2004).

Table 3. Paleomagnetic chronostratigraphical markers (tie points) based on the correlation between the 12CS and 02CS cores presented in this study, with other paleomagnetic records (Nettilling Lake, Beaudoin et al., 2016) and geomagnetic field models (GUMF1, Jackson et al., 2000; and CALS3k.4, Korte & Constable, 2011) calculated for the study area.

Tie points	Depth 02PC (cm)	Depth 02CS* (cm)	Depth 12PC* (cm)	Depth 12CS (cm)	Median (a) Age Cals3K.4	GUMF1	Nettilling Lake	Median age	SD
I1			62	62	−20	−25	4.4	−20	10
I2	28	21	183	263	130	132.5	127.75	130	10
I3			223	343	230	236		233	10
I4	46	36	270	419	340	319.5	339.6	340	8
I5			328	517			409.1	402	6
I6			374	552			460.9	461	6

*Depth RDLs free.

the two $\triangle R$ estimates and the large 2σ uncertainties illustrate the inherent variability in the local marine $\triangle R$ of glacier-influenced fjords (e.g. Russell et al., 2011).

Age modeling

Prior to the construction of age–depth models, the correlation of the k_{LF} and log(Zr/Zn) profiles of cores 12TWC/PC, 05BC and 02PC was conducted to estimate the absence and deformation of sediments at the tops of the piston cores (Supporting Information Fig. S4). These correlations suggest that (i) ~3 cm of sediments at the top of core 02PC were lost during piston coring; (ii) no sediments were lost due to coring at the top of core 12PC; and (iii) the uppermost parts of cores 12PC and 02PC show deformations at ~50 and 42 cm, respectively, which is related to the cumulative action of compaction and stretching during piston coring (Fig. S1). Thus, the depths of the piston cores were adjusted accordingly. In this context, since the box and trigger weight corers are designed to recover a relatively undisturbed sample of the sediment–water interface, cores 12PC/TWC and 05BC and 02PC were combined into two composite sequences (hereafter referred to as 12CS and 02CS) based on the correlation of the k_{LF} and log(Zr/Zn) profiles (Fig. S4). Indeed, the upper 50 cm of core 12CS corresponds to core 12TWC, and the rest of the sequence corresponds to core 12PC (50–609 cm). In contrast, in core 02CS, the upper 42 cm corresponds to core 05BC, and the rest corresponds to core 02PC (42–228 cm). The depths of these composite sequences were adjusted, and the age–depth models were generated using the corrected composite depths. To derive the best age–depth model, we used the R package 'rbacon' version 2.5.7 (Blaauw & Christen, 2011), as this

program allows (i) the incorporation of other chronostratigraphic markers (such as ^{210}Pb and $^{239+240}$Pu dating obtained from the 'serac' R package and paleomagnetic tie points) and (ii) the estimation of the best fit or weighted mean age for each depth with a 95% confidence interval using a Bayesian approach. Although 'rbacon' produces a robust age model for cores 12CS and 02CS, we recognize the difficulties associated with establishing accurate age–depth models in marine sediment cores (e.g. Telford et al., 2004; Trachsel & Telford, 2017; Lacourse & Gajewski, 2020).

Statistical approach

The qXRD and pXRF data were analyzed using a compositional data approach, which allows evaluation of data subjected to a constant-unit sum (Aitchison, 1982). For statistical analysis, we followed the approach presented in Montero-Serrano et al. (2010), Schmidt et al. (2019) and Corminboeuf et al. (2021a,b). R software (R Core Team, 2021) was used to perform all statistical analyses. First, values below the detection limit were imputed via multiplicative lognormal replacement with the 'zCompositions' package (Palarea-Albaladejo & Martin-Fernandez, 2015) to preserve the geometry of the compositional data while accounting for corresponding detection limit thresholds. Second, a log-centered (clr) transform was applied to the data with the 'compositions' package (van den Boogaart & Tolosana-Delgado, 2008) to allow the valid application of classical (Euclidean) statistical methods to the compositional data (Aitchison, 1982; Montero-Serrano et al., 2010). Next, principal component analysis (PCA) was performed on qXRD and pXRF data to identify mineral & chemical associations with similar relative variations (e.g. von

Eynatten et al., 2003; Montero-Serrano et al., 2010). PCA was conducted with the 'compositions' (van den Boogaart & Tolosana-Delgado, 2008) and 'factoextra' packages (Kassambara & Mundt, 2020).

Results and interpretation

General grain size, mineralogical and geochemical characteristics

The grain size distributions of cores 12CS and 02CS indicate a composition that is generally dominated by silts and clays, with some intervals composed of medium to coarse sand (Fig. 3). The grain size frequency distributions of these coarse-grained samples show a unimodal shift toward higher values, indicating better sorted sediments and different depositional regimes (Fig. 3A, B). The vertical profiles of D90 show that these coarse-grained intervals are characterized by values of up to 67 and 120 μm in cores 12CS and 02CS, respectively (Fig. 4). IRD is abundant in core 12CS, with the highest concentrations in the interval between 250 and 500 cm, while core 02CS shows very low IRD counts.

We tested the correlation between $\overline{SS}$ and SS% to evaluate whether the sortable silt record in cores 12CS and 02CS was sufficiently current-sorted to provide a reliable bottom flow history (McCave & Andrews, 2019a,b). A good positive coefficient of correlation was obtained for both composite sequences ($r = 0.86$, $n = 240$ for 12CS and $r = 0.94$, $n = 89$ for 02CS) (Supporting Information Fig. S6A, C). Likewise, 90% of the data have a five-point running down-core correlation (r_{run}) between $\overline{SS}$ and SS% of >0.5 (Fig. S6B, D). These results suggest that much of the sortable silt records in cores 12CS and 02CS are current-sorted, mainly driven by changes in the hyperpycnal flow speed.

The boxplot of bulk mineralogical and geochemical data from cores 12CS and 02CS are shown in Fig. 5A and B. The mineralogy of the bulk sediment fraction from Coronation Fjord is dominated by Pl (25–32%), Kfs (24–33%), Qz (13–35%), Chl (1.5–14%) and Bt (0.5–10%), and by lower proportions (<5%) of detrital carbonates, Fe-bearing minerals, Am and Px (Fig. 5A; Supporting Information Fig. S5). In general, Pl, Kfs, Qz, Chl and Bt represent more than 90% of the overall mineral concentration in both sediment cores. These mineralogical results are consistent with those reported for surface sediments from Coronation, Maktak and Pangnirtung Fjords (Andrews et al., 2018; Andrews, 2019). Furthermore, the major element compositions of bulk sediments in cores 12CS and 02CS are dominated by Si (~0.3–9%), Fe (~0.5–2.5%), K (~0.1–1.5%), Al (~0.3–2%), Ca (~0.2–1.5%) and Ti (~0.03–0.3%), while Mn, Zn, Rb, Y, Sr and Zr show lower concentrations (0.001–0.08%) (Fig. 5B).

Because of the similarity in the mineralogical and geochemical compositions of cores 12CS and 02CS (Fig. 5A, B), PCA was conducted with both cores together (Fig. 5C, D). For the two cores, PCA of the qXRD data indicates that PC1 (89% of the total variance) is positively associated with Pl, Kfs and Qz and negatively associated with Chl and Bt, whereas PC2 (9.1% of the total variance) is positively associated with Bt, Kfs, Pl and Qz and negatively associated with Chl (Fig. 5C). PCA of the pXRF data reveals that PC1 (41% of the total variance) is positively associated with Zr, Sr, Rb, Y, Zn, Fe and Mg and negatively associated with Si, Al, K, Ti and Ca; PC2 (31.5% of the total variance) is positively associated with Si, Zr, K, Ca, Sr and Y and negatively associated with Zn, Fe, Rb, Ti, Al and Mg (Fig. 5D).

These results reveal a similar mineral composition in both ice-proximal (12CS) and ice-distal (02CS) zones of Coronation Fjord (Supporting Information Fig. S7). Therefore, it is not possible to discriminate the variations in the detrital contribution of each fjord in core 02CS (Fig. 2A). Based on these results, we selected Chl+Bt/Kfs+Pl and Qz/Kfs+Pl to trace changes of detrital input from the Canadian Shield over time in terms of clay and feldspar mineral inputs (Fig. 4E, F, M, N). Additionally, the log(Fe/Ca) ratio was used to represent variations in terrigenous sediment delivery based on the abundance of Fe in clay minerals and Ca in plagioclase facies
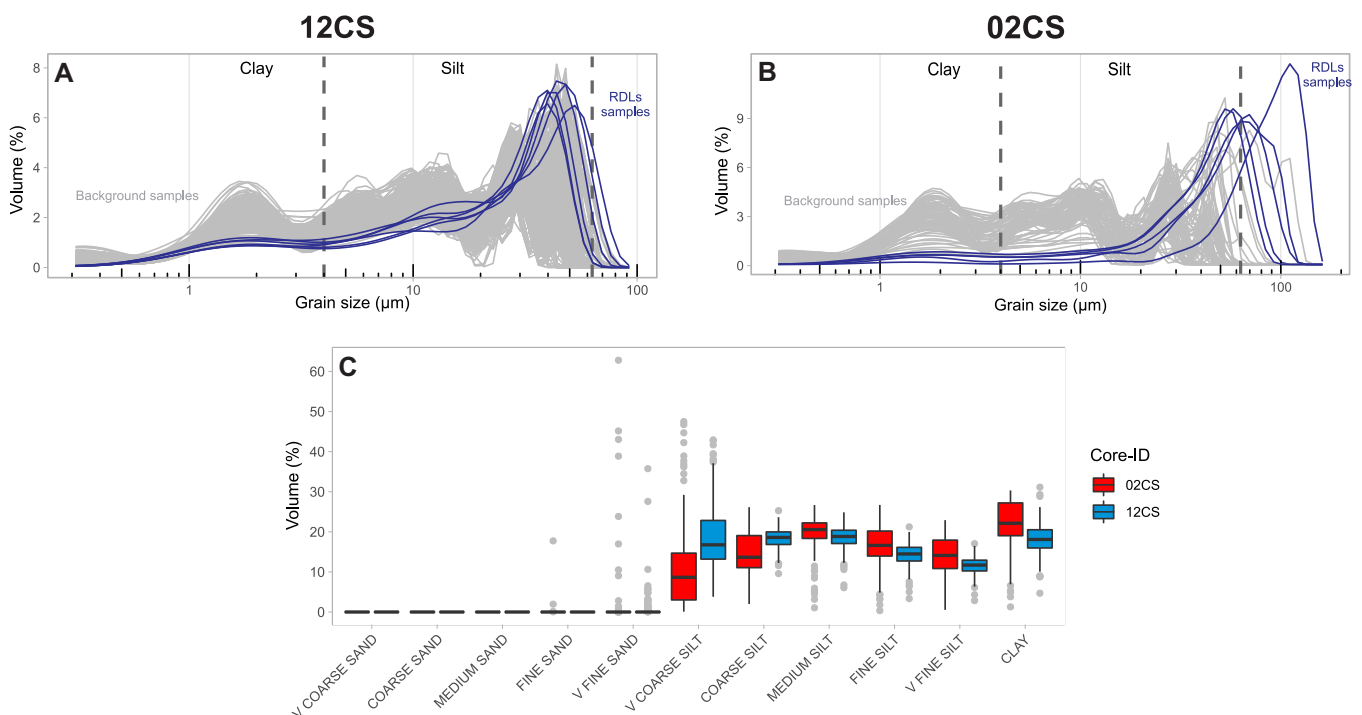
Figure 3. Frequency curves of raw grain size data for cores 12CS (A) and 02CS (B); (C) boxplot of the grain size distribution (%) for both cores. [Color figure can be viewed at wileyonlinelibrary.com]
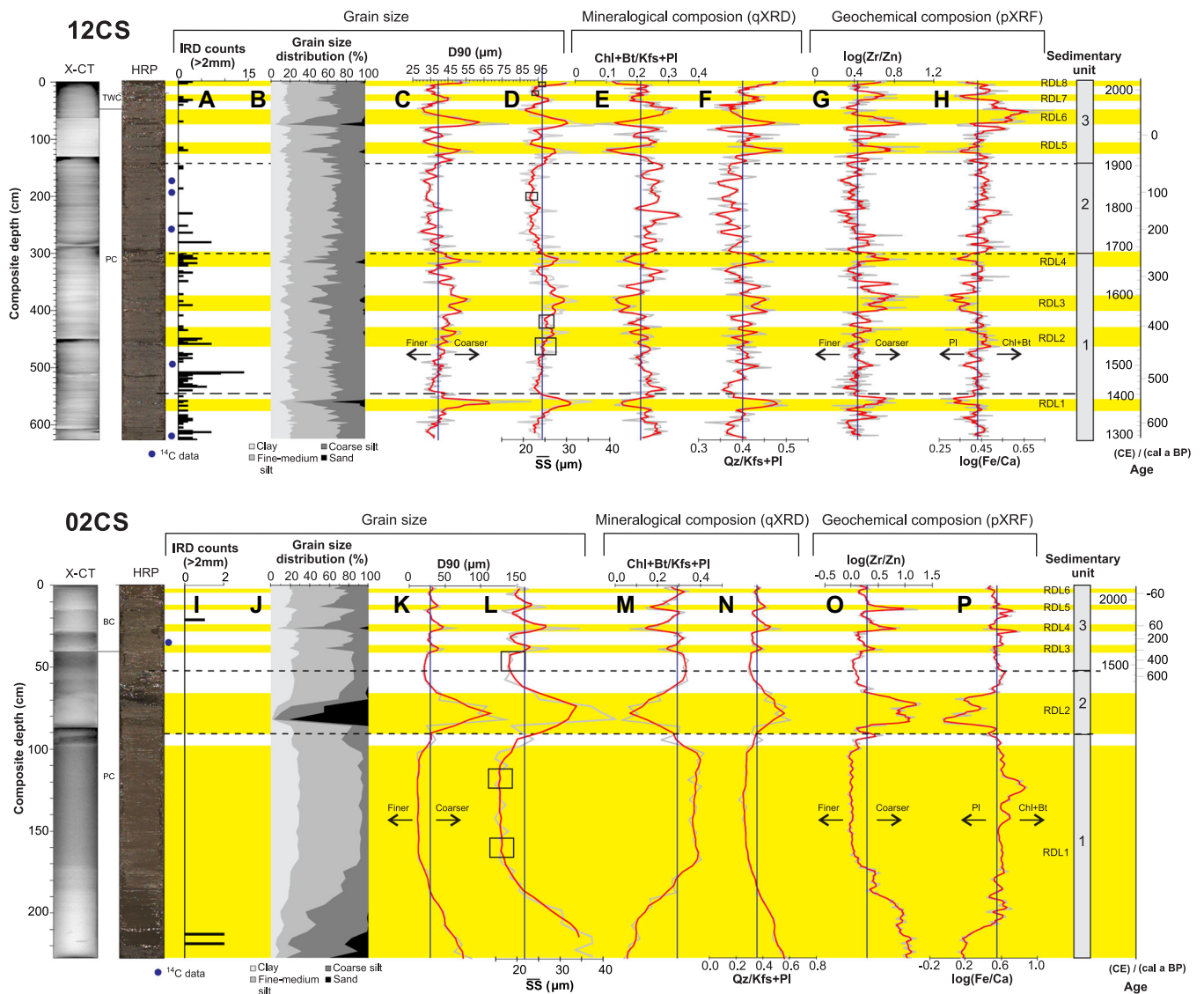
Figure 4. X-CT scan image, high-resolution core photography, grain size distribution, D90, mean size of sortable silt fraction $\overline{SS}$, mineralogical and chemical tracers, and sedimentary units of cores 12CS and 02CS. RDLs are numbered and highlighted in yellow. The black vertical line represents the median of the data for each proxy. Black boxes indicate sections of the sortable silt record that do not pass the reliability test of a down-core correlation coefficient >0.5 between $\overline{SS}$ and SS% (McCave & Andrews 2019a). [Color figure can be viewed at wileyonlinelibrary.com]

(Fig. 4H, P; Adgebie et al., 2003; Croudace & Rothwell, 2015). The log(Zr/Zn) ratio was used as a semiquantitative grain size indicator (von Eynatten et al., 2012; Croudace & Rothwell, 2015; Wu et al., 2020) with a better vertical resolution than discrete grain size analysis. In this case, Zr is associated with coarse weathering-resistant mineral facies, and Zn is linked to fine-grained clay minerals (Fig. 4G, O). pXRF elemental ratios are presented as log ratios to mitigate the amplitude changes in elemental concentrations caused by variable water contents, grain size distributions and irregularities of the split core surface (e.g. Weltje & Tjallingii, 2008).

Rapidly deposited layers and magnetic properties

Based on physical, magnetic and sedimentological data, eight RDLs were identified in core 12PC, and six RDLs were identified in core 02PC (Fig. 6). These RDLs were recognized by low cohesive material with a soupy texture, generally coarse-grained basal layers, an upward increase and then decrease in D90 and $\overline{SS}$ values, low L* values, peaks in wet bulk density and k_{LF}, low basal paleomagnetic inclinations and

low k_{ARM}/k_{LF} values. Lower paleomagnetic inclinations are associated with energetic depositional processes where the magnetic particles are plastered horizontally because of high flow velocity and rapid sediment accumulation (e.g. St-Onge et al., 2004). We identified two types of RDL based on digital X-radiographs and high-resolution grain size analyses (Fig. 7). The first type (RDLs 1–3 in core 12CS; Figs. 4, 6 and 7) have a thickness between 15 and 25 cm and is recognized by a laminated coarsening-upward unit, followed by a thick fining-upward unit. This type of deposit is interpreted as deposits from hyperpycnal turbidity currents or hyperpycnites (Mulder et al., 2003). The second type (RDLs 4–8 in core 12CS and RDLs 1–6 in core 02CS; Figs. 4, 6 and 7) consists of 3- to 120-cm-thick fining-upward to homogeneous clayey silt units interpreted as classical turbidites (Bouma, 1962). This transition is interpreted as the completion of the deposit due to the decrease in flow velocity.

Outside of the RDLs, the inclination values oscillate around the expected value for the coring site and were calculated according to the geocentric axial dipole model (I_{GAD}, 78.17°N for Coronation Fjord), denoting a well-recorded paleomagnetic signal for both cores (Fig. 6; Stoner & St-Onge, 2007).
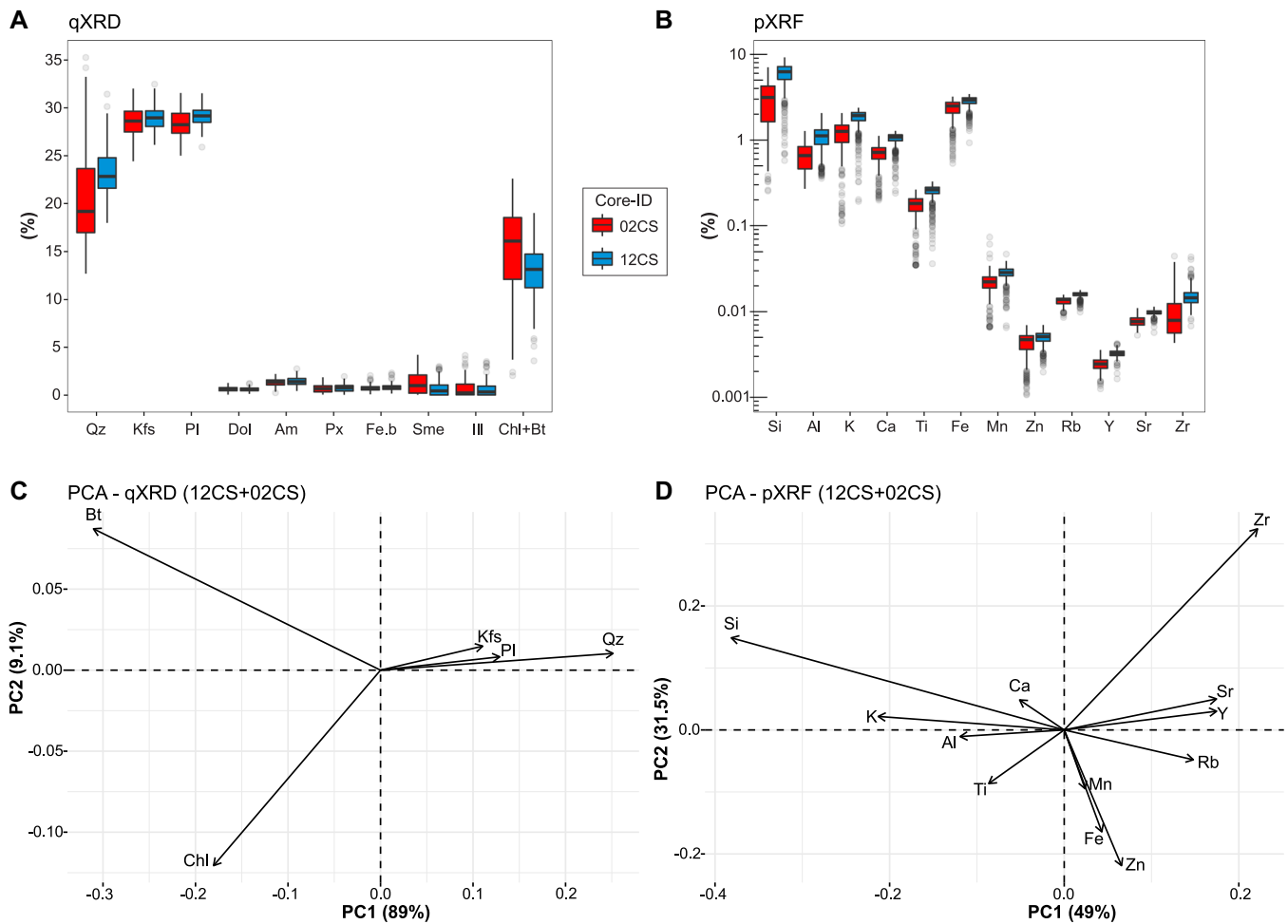
Figure 5. Results of mineralogical and chemical composition for cores 12CS and 02CS. (A) Boxplot of the distribution of the main minerals (wt.%); (B) boxplot of the chemical composition distribution (%). Note that the relative concentrations obtained with the pXRF sensor were converted to percentage (1% = 10 000 ppm) for better visualization. (C) Biplots of the PCA of the bulk mineralogical data; (D) biplots of the PCA of geochemical data. [Color figure can be viewed at wileyonlinelibrary.com]

The down-core MAD values oscillate at ~5° (except in the RDL intervals), which indicates high-quality directional data (Stoner & St-Onge, 2007; Fig. 6). The pseudo-S ratio ($IRM_{0mT}/SIRM0_{mT}$) varies between 0.96 for core 12CS and 0.99 for core 02CS. Values > 0.9 indicating low coercivity minerals such as magnetite (Stoner & St-Onge 2007).

Chronology

The chronological framework of core 05BC is limited by the occurrence of RDLs. The log(Zr/Zn) and grain size (D90 µm) data led to the identification of four layers (2–3, 12–14, 23–25 and 36-40 cm; Fig. 4; Supporting Information Fig. S1A). As these RDLs are considered to be instantaneous deposits, they were excluded to build an event-free sedimentary record (Fig. S1A). $^{210}Pb_{excess}$ activities plotted on a logarithmic scale reveal three linear trends that suggest three mean sediment accumulation rates (SARs) of 0.67 cm a^{-1} below 16 cm, 0.12 cm a^{-1} between 11 and 16 cm, and 0.42 cm a^{-1} in the uppermost part of the sequence (0-11 cm; corresponding to the period from 1994 to 2018 CE; Fig. S1A). This age–depth model is well constrained by $^{239+240}Pu$ dates and one AMS ^{14}C date at 18 cm (1955–1958 CE). The $^{239+240}Pu$ profile shows an onset of deposition at 18.5 cm and a peak at 16.5 cm (Fig. S1D), which correspond to the years where this radionuclide was introduced into the atmosphere with atmospheric nuclear testing in 1952 and peaked at the height of testing in 1963 (Ketterer et al., 2002, 2004). On this basis, core 05BC spans the last 170 years, from ~1848 to 2018 CE (Fig. S1A). The four RDLs observed in core 05BC are dated to 2013–2015, 1990–1997, 1916–1936 and 1860–1866 CE.

In core 12TWC, the total ^{210}Pb activity shows 'event horizons' with irregular ^{210}Pb variations that could indicate varying ^{210}Pb fluxes due to meltwater flood events (Supporting Information Fig. S2; e.g. Xu et al., 2015; Arias-Ortiz et al., 2018). Therefore, ^{210}Pb data from core 12TWC were not considered in developing the composite age model of core 12CS.

Paleomagnetic chronological markers were obtained by comparing the event-free inclination profiles obtained for each core versus depth to global geomagnetic field models (GUMF1, CALS3k.4, CALS10k.2; Jackson et al., 2000; Korte & Constable, 2011; Constable et al., 2016) or previously published records (Nettilling Lake; Beaudoin et al., 2016). Based on similar shifts in the Earth's magnetic field behavior in the different records, six chronostratigraphic markers (tie points) were determined (Fig. 8A–D, F–I; Table 3). These tie points were then used in the construction of an age–depth model. The age–depth model indicates that core 12PC spans the last 600 cal a BP, and the calculated sedimentation rates range from ~0.6 cm a^{-1} (626–175 cm depth), ~0.8 cm a^{-1} (175–70 cm depth) to 0.9 cm a^{-1} (top 70 cm) (Fig. 8D, E). Core 02PC spans the last 500 cal a BP, and the calculated sedimentation rate ranges from 0.06 cm a^{-1} (50–20 cm depth), 0.12 cm a^{-1} (20–10 cm depth) and increases to 0.4 cm a^{-1} in the top 10 cm (Fig. 8I, J).
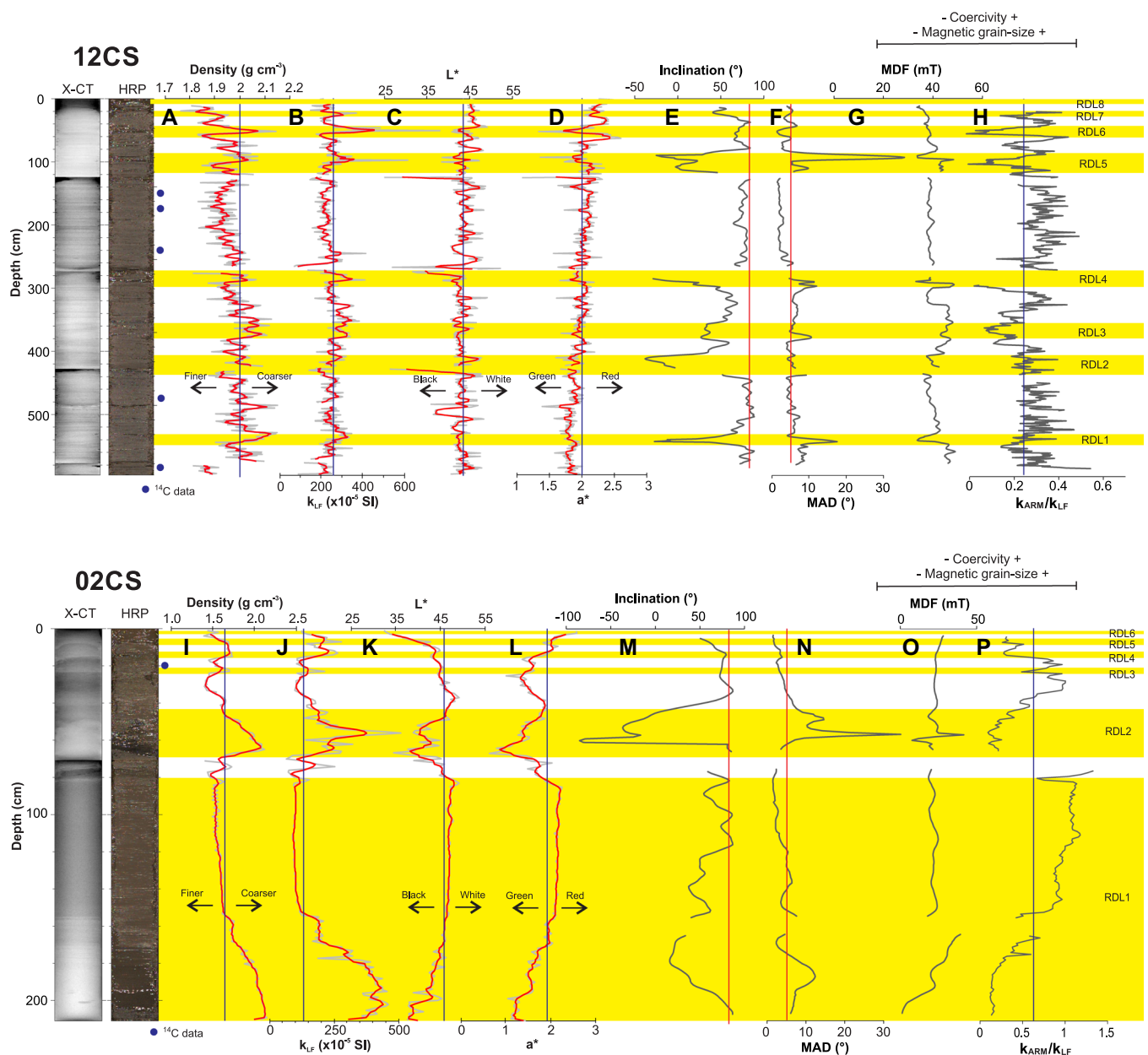
Figure 6. Down-core variations in cores 12PC and 02PC, showing X-CT images, high-resolution core photography, grain size parameters, IRD counts (>2-mm fraction), wet bulk density, magnetic susceptibility (k_{LF}) and magnetic properties (inclination, MAD, MDF and k_{ARM}/k_{LF}). RDLs are numbered and highlighted in yellow. The vertical red line delineates an MAD value of 5°. The black vertical line represents the median of the data for each proxy. [Color figure can be viewed at wileyonlinelibrary.com]

Sedimentary units

Sedimentary units were determined on the basis of visual core descriptions, high-resolution core photography, X-CT scan images, physical properties, grain size parameters, and mineralogical and geochemical data (Fig. 4). Considering these observations, cores 12CS and 02CS show three distinct units. These units, labeled 1–3 in core 12CS and 02CS from base to top, are described and interpreted below according to core depths (Figs. 4 and 9).

Core 12CS

Unit 1 (626–300 cm) is mainly composed of grayish brown (10YR 5/2) clayey silts with brown (10YR 5/3) silty to sandy subcentimeter-scale laminations and disseminated gravel-sized clasts (interpreted as IRD). The gravel-sized clast content decreases toward the top of the unit. Unit 1a (626–550 cm) is characterized by high Chl+Bt/Kfs+Pl and log(Zr/Zn) values and

lower Qz/Kfs+Pl and log(Fe/Ca) values (Fig. 4). A cross-laminated interval is found between 566 and 543 cm and coincides with an increase in D90 and $\overline{SS}$ values, as well as a decrease in inclination, MDF and k_{ARM}/k_{LF} ratio values (RDL 1 interval; Fig. 6). Most of the RDLs identified in this unit are of the reverse-to-normal grading type (Fig. 7). A distinct layer with clasts that is well stratified is observed between 498 and 480 cm.

Unit 2 (300–140 cm) is composed of grayish brown (10YR 5/2) laminated clayey silts with brown (10YR 5/3) sediments with low IRD counts. The grain size distribution shows relatively more fine material with below-median values of bulk density, D90, $\overline{SS}$, Qz/Kfs+Pl, a* and log(Zr/Zn) ratios. The unit contains no RDLs, as indicated by a stable signal in paleomagnetic parameters (inclination, MAD and MDF; Fig. 6).

Unit 3 (140–0 cm) is composed of grayish brown (10YR 5/2) laminated mud with low IRD abundance. In contrast to Unit 2, Unit 3 consists of stratified muddy silt layers that are 1–2 cm thick. Unit 3 presents the largest fluctuations in the values of
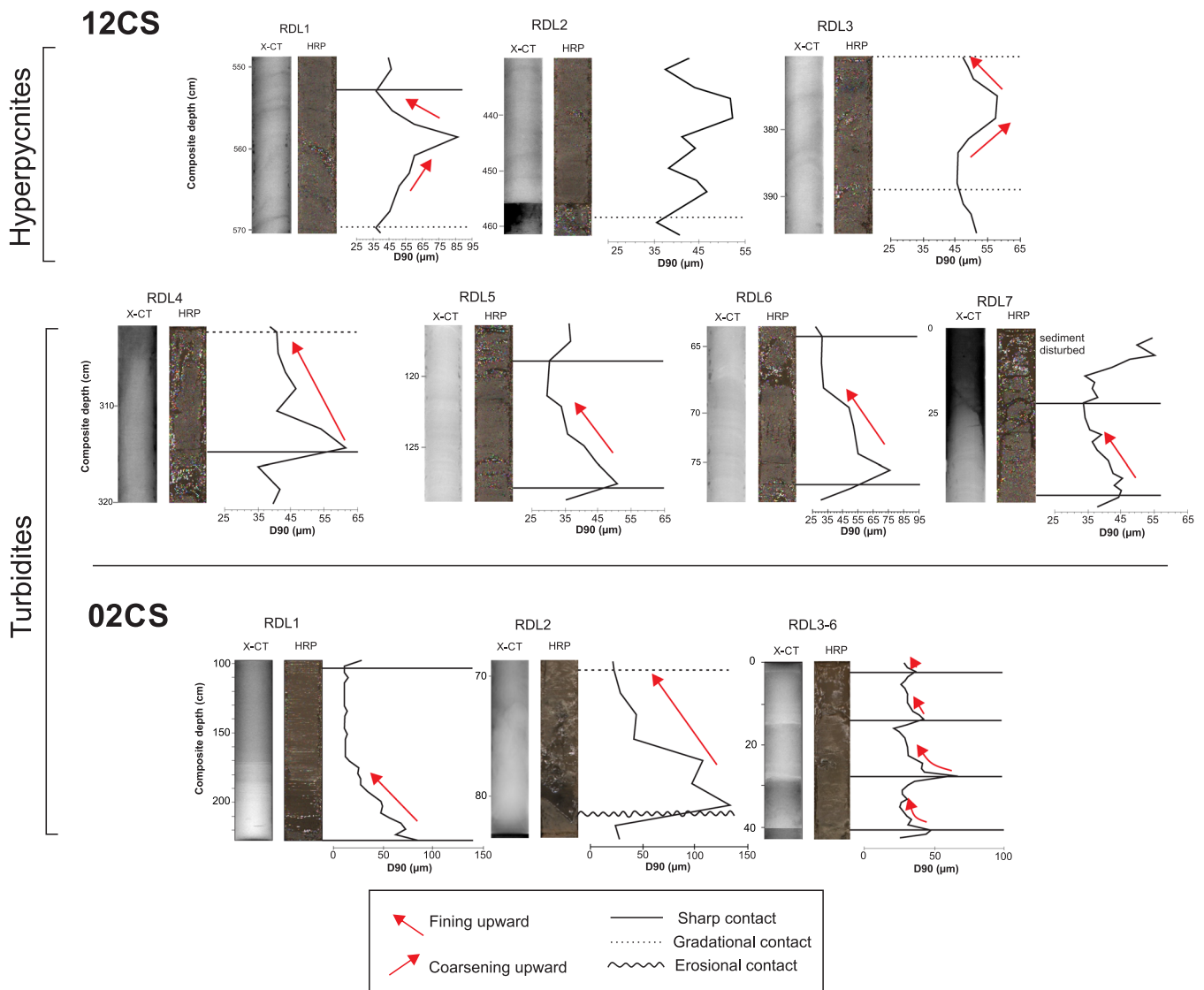
Figure 7. X-CT scan image, high-resolution core photography and grain size trend (D90) for the fining-upward turbidite and hyperpycnal deposit sequences identified in cores 12CS and 02CS. [Color figure can be viewed at wileyonlinelibrary.com]

the various measured parameters. Detrital proxies, such as wet bulk density, k_{LF}, log(Zr/Zn) and log(Fe/Ca), show high values with occasional peaks (Figs. 4 and 6). These variations coincide with the presence of several RDL intervals of fining-upward type.

Core 02CS

Unit 1 (225–100 cm), in the interval between 225 and 170 cm, is composed of gray (7.5YR 5/1) sandy silts with disseminated IRD that grades toward the top to clayey silts (7.5YR 5/2 brown) that are finely laminated. The gradation in grain size is corroborated by a decrease in parameters, such as wet bulk density, k_{ARM}/k_{LF}, Qz/Kfs+Pl and log(Zr/Zn), to the top of the record (Figs. 4 and 6). The interval between 170 and 100 cm is mainly composed of homogenous brown (7.5YR 5/2) silty clay. The lower D90, $\overline{SS}$, wet bulk density and k_{LF} values suggest that the grain size distribution is dominated by a high proportion of fine-grained sediments (Figs. 4 and 6). This interval is also characterized by an increase in Chl+Bt/Kfs+Pl and log(Fe/Ca) ratios and in L* and a* values. All detrital proxies are constant throughout the interval between 190 and 100 cm, corroborating its homogeneous character. This unit represents the fining-upward RDL type, although the base of this unit might be missing.

Unit 2 (100–50 cm) is composed of grayish brown (2.5YR 5/2) sandy mud. The high D90 values dominate at the base of this unit, indicating a high proportion of medium- to coarse-grained sediments (Fig. 4). The presence of cross-lamination at the base of this unit and normal grading suggest an instantaneous turbidite deposit (e.g. Powell, 1985). This turbidite deposit is also corroborated by a sudden upward increase and then decrease in $\overline{SS}$ values within the unit, an increase in wet bulk density, k_{LF}, Qz/Kfs+Pl and log(Zr/Zn), and the fact that these values gradually decrease toward the top of the record (Figs. 4 and 6). This interval is also accompanied by shifts to low inclination and k_{ARM}/k_{LF} values.

Unit 3 (50–0 cm) is composed of grayish brown (10YR 5/2) mud that is moderately bioturbated (based on the X-CT scan images). Moreover, this unit is characterized by the presence of a succession of RDLs. The coarser base of each RDL is visible on the X-CT scan images. These intervals are characterized by a sharp contact with rapid upward increase and then decrease in coarse silts, fine sands, $\overline{SS}$, Qz, Kfs+Plg and log(Zr/Zn) (Fig. 4), which can be interpreted to reflect the waxing followed by waning flow conditions during large glaciogenic meltwater discharge events. Thus, the presence of these RDLs suggests that glacial turbidite plumes dominated in this interval.
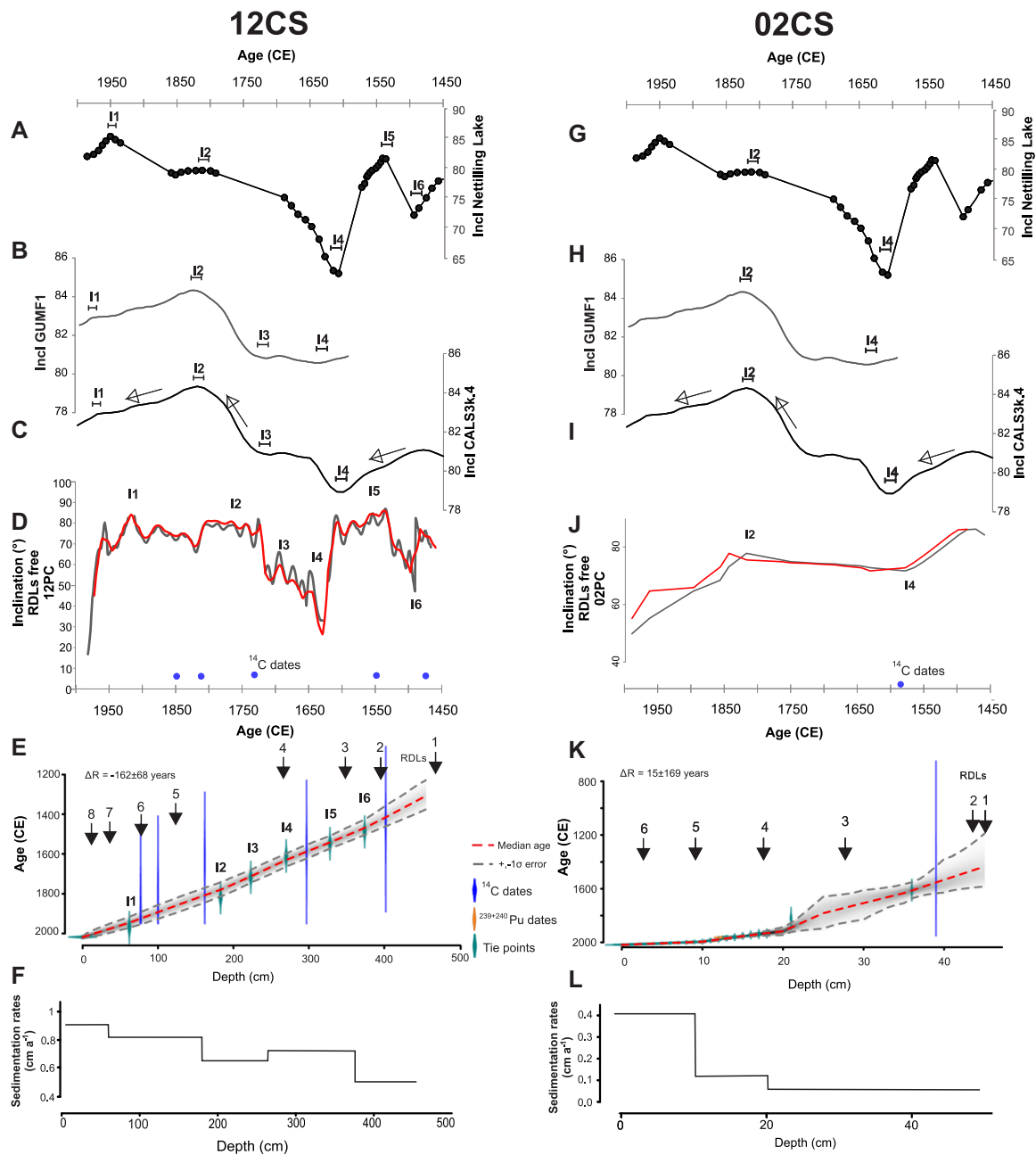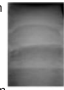
Figure 8. Comparison of the inclination values from sediment cores (D) 12PC and (J) 02PC compared to (A, G) Nettilling Lake (Beaudoin et al., 2016), (B, H) GUMF1 (Jackson et al., 2000) and (C, I) CALS3k.4 (Korte & Constable, 2011) geomagnetic field models. (D, J) Composite age model using ^{210}Pb, $^{239+240}$Pu and ^{14}C ages, and paleomagnetic tie points. The Bayesian age–depth model was constructed using the R package BACON (Blaauw & Christen, 2011). The red dashed line shows the best age model, and the gray shading represents the chronological uncertainties (95% confidence interval). Black arrows show the RDL ages. (E, J) Estimated sedimentation rates (cm a^{-1}). [Color figure can be viewed at wileyonlinelibrary.com]

Discussion

Sedimentological interpretation of rapidly deposited layers

Detrital proxies from cores 12CS and 02CS suggest that RDLs occur frequently in both ice-proximal (eight RDLs) and ice-distal (six RDLs) environments of Coronation Fjord as well as over time (Figs. 4 and 6). However, there are different triggering mechanisms that may be responsible for RDL deposition in these proximal and distal glacial settings. In the ice-proximal environment, several glacial sedimentary processes, such as glaciogenic debris flows, icebergs and sea ice rafting, meltwater plumes and turbidity currents, can influence marine sedimentation (Powell, 1985; Cowan & Powell, 1991; Ó Cofaigh et al., 2013; Dowdeswell et al., 2015). The presence of a submarine channel with bedforms along with high-amplitude parallel reflections in an ice-proximal environment (Fig. 2D) indicates that sedimentation is mainly controlled by meltwater discharge. In core 12CS, all RDLs are characterized by finely laminated glaciomarine sediments that are rich in Qz, Kfs and Pl. However, the structure of RDLs 1–3 is typical of hyperpycnites, with a reverse-to-normal graded deposit (Figs. 4C, D and 7). This type of deposit can be formed from flood-induced currents carrying a high load of particles, generating a waxing following by a waning flow (e.g. Mulder & Syvitski, 1995; Mulder et al., 2003; Duboc et al., 2017). These flows can occur during a single cycle of glaciogenic meltwater discharge as well as during river floods caused by seasonal and/or catastrophic events; however, in this setting, they are more probably related to meltwater discharge from the tidewater glacier. Conversely, the structure of RDLs 4–8 is typical of classical turbidites (Figs. 4C, D and 7).

Core	Units	X-ray	Image	Lithofacies	Colour	Sedimentary structures	D90 (μm)	Depositional processes
02CS	Unit 3	0cm / 30cm		Mud moderately bioturbated with turbidites succession	10YR 5/2 grayish brown	Stratified mud moderately bioturbated	28	Turbidity currents and meltwater plumes
	Unit 2	45cm / 70cm		Sandy mud	2.5YR 5/2 grayish brown	-Convolute lamination? -Graded toward the top	68	Outburst flood hyperpycnal flow
	Unit 1	100cm / 140cm / 160cm		Homogeneous mud	7.5YR 5/2 brown	-Massive mud -No apparent structure or bioturbation are observed	13	Outburst flood hyperpycnal flow
		203cm		Sandy mud with disseminated clasts	Intercalations 7.5YR 5/2 brown 7.5YR 5/1 gray	-Disseminated clasts -Graded toward the top	44	
12CS	Unit 3	60cm / 120cm		Laminated mud with IRDs	10YR 5/2 grayish brown	Rhythmic succession of clay and silt laminae	38	Turbidity current, ice rafting and meltwater plumes
	Unit 2	200cm / 250cm		Laminated mud with absence of RDLs	10YR 5/2 grayish brown	Parallel laminations	35	Meltwater plumes
	Unit 1	350cm / 400cm / 570 cm / 590cm		Laminated mud with IRDs	10YR 5/2 grayish brown	-Parallel laminations - IRD layer / -Parallel laminations -Cross-laminations -Dispersed IRDs	40	Turbidity current, ice rafting and meltwater plumes

Figure 9. Summary of the physical characteristics, average grain size and interpretation of the depositional processes of lithofacies identified in cores 12CS and 02CS. [Color figure can be viewed at wileyonlinelibrary.com]

In these cases, the flood-induced currents decelerated with time, depositing the so-called normally graded sequence (Bouma, 1962). However, the lower inversely graded sediment could have been eroded by the peak flow (Mulder et al., 2001), preserving only the normally graded sand layer. Hence, both types of RDLs could be formed by hyperpycnal flows of sediment-laden meltwater associated with the Coronation Glacier dynamics. In fact, glacial erosion typically generates a large amount of glaciogenic sediment (rock flour), which can then be transported by meltwater streams and by hyperpycnal currents into the fjord (e.g. Dowdeswell et al., 2015; Stevenard et al., 2022). In addition, enhanced calving activity in an ice-proximal environment can generate turbulence in the fjord floor, which in turn promotes submarine landslides and gravity flows (Powell, 1985; Normandeau et al., 2021). This mechanism could also have influenced the sedimentary dynamics during the deposition of RDLs 1–4 in Unit 1 of core 12CS, where the abundance of IRD suggests enhanced calving activity (Fig. 4A).

In the ice-distal environment (core 02CS), RDLs 1 and 2 are coarser-grained with low L* and a* values (suggesting dark sediments that are richer in organic matter; Debret et al., 2011; Supporting Information Fig. S8) and are relatively thick (38–42 cm). The facies of these RDLs suggest the rapid deposition of a large amount of sediment in the fjord that could be associated with glacial outburst flood events (GOFs; Emmer, 2017). In glacier-influenced fjords, GOFs are often

caused by the catastrophic drainage of proglacial lakes from the retreat of ice sheets (e.g. Emmer, 2017; Vandekerkhove et al., 2021). These deposits are also identified in the sub-bottom profile of the ice-distal environment (Fig. 2E), and are characterized by thick transparent acoustic facies, with a higher frequency towards the top. However, intense precipitation, rain-on-snow events or high seasonal meltwater discharge can also result in sediment discharge peaks termed meteorological outburst floods (e.g. Vandekerkhove et al., 2021, Liu et al., 2021). In Chilean Patagonia, recent studies show that GOFs are recorded in downstream fjord sediments as fine-grained and organic-poor layers, representing the high amount of glacier rock flour transported during lake outbursts, whereas meteorological floods are represented by coarser and organic-enriched deposits (Vandekerkhove et al., 2021, Liu et al., 2021). Based on these previous studies, and considering the sedimentological characteristics of RDLs 1 and 2, we speculate that the meteorological floods sourced from Maktak and North Pangnirtung Fjords (which deliver sediments via proglacial rivers; Fig. 2) may have triggered these RDL deposits. On the satellite images (Fig. 2A) it is possible to distinguish an upper sandur delta formed in North Pangnirtung Fjord, which is blocked by a large deposit, previously interpreted by Dyke et al. (1982) as a ground moraine and more recently as a large landslide by Syvitski and Normandeau (2023). It is possible that the sandur delta north of this deposit filled a lake, the latter episodically leading to

outbursts, forming the GOFs at the intersection of the three fjords. Alternatively, the GOFs could also originate from subglacial meltwater discharges from Coronation or Maktak Fjords. This is less evident for RDLs 3–6 in core 02CS (Figs. 4 and 6). Indeed, the facies (i.e. laminated muds that are rich in Qz, Kfs and Pl), low thicknesses (1–3 cm) and high frequency of these RDLs seem to indicate that turbid hyperpycnal meltwater plumes sourced from the three fjords (Coronation, Maktak and North Pangnirtung) are driving these events.

There are also some physical factors (e.g. seafloor morphology, slope, presence/absence of channels and ice fluxes) that may favor the occurrence of outburst floods and turbidity currents in the distal environment in Coronation Fjord. The position of core 02CS at the junction of the three fjords probably records sediment inputs from all of them. Satellite images show that large sediment plumes can influence sedimentation at the location of core 02CS (Fig. 2A). Likewise, Maktak and North Pangnirtung Fjords are considered to be mature because their glaciers have receded and present large sandur surfaces (Gilbert, 1983) and they both consist of sediment waves and chutes and channels delivering sediment through turbidity currents (Syvitski & Normandeau, 2023). In fact, these sandur deltas do not prograde much into the fjord as most of their sediment load bypasses the foreset zone to reach the basin. The exposed sediments from the sandur surfaces are susceptible to easy remobilization and transport by freshwater inputs from winter remnant glacier melt and rain storms (Syvitski & Shaw, 1995). Therefore, sediment delivery in Maktak and North Pangnirtung Fjords may be even higher than in Coronation Fjord. This can be evidenced by the highest values of log(Fe/Ca) in core 02CS compared to in 12CS (Fig. 4H, P). Indeed, an enhanced input of iron-bearing sediments from the sandur surface can increase the Fe concentrations in the sediments supplied to the distal zone. In this context, we hypothesize that more intense warm summer periods probably promoted large hyperpycnal flows of sediment-laden glacial meltwater in the three fjords, which in turn generated turbidite deposits in the conjunction zone (Figs. 2A and 13). Moreover, the conjunction zone is preceded by a slope of ~4.57°, which can favor the transport of gravity

flows into the deeper zone of the basin (Pope et al., 2019). The formation of scour structures along the slope (Fig. 2C) indicates a significant current flow along the slope, which can also promote turbidite deposition (Ben Meftah et al., 2020). Thus, it is evident that turbidites, gravity flows and meteorological outburst floods are important sediment delivery mechanisms in Coronation Fjord. However, more studies of the high-resolution bathymetry of the Maktak and North Pangnirtung Fjords are needed to determine whether other physical bathymetric features may control sediment transport into the fjord.
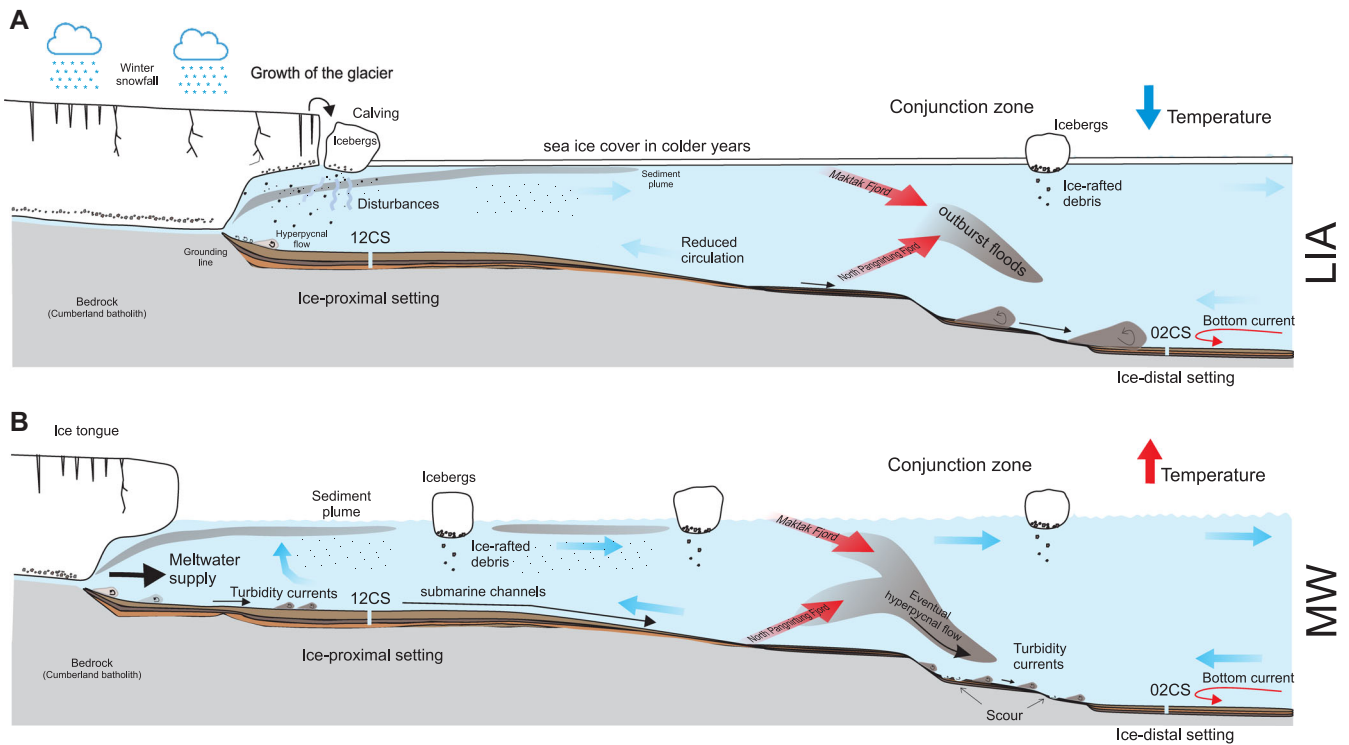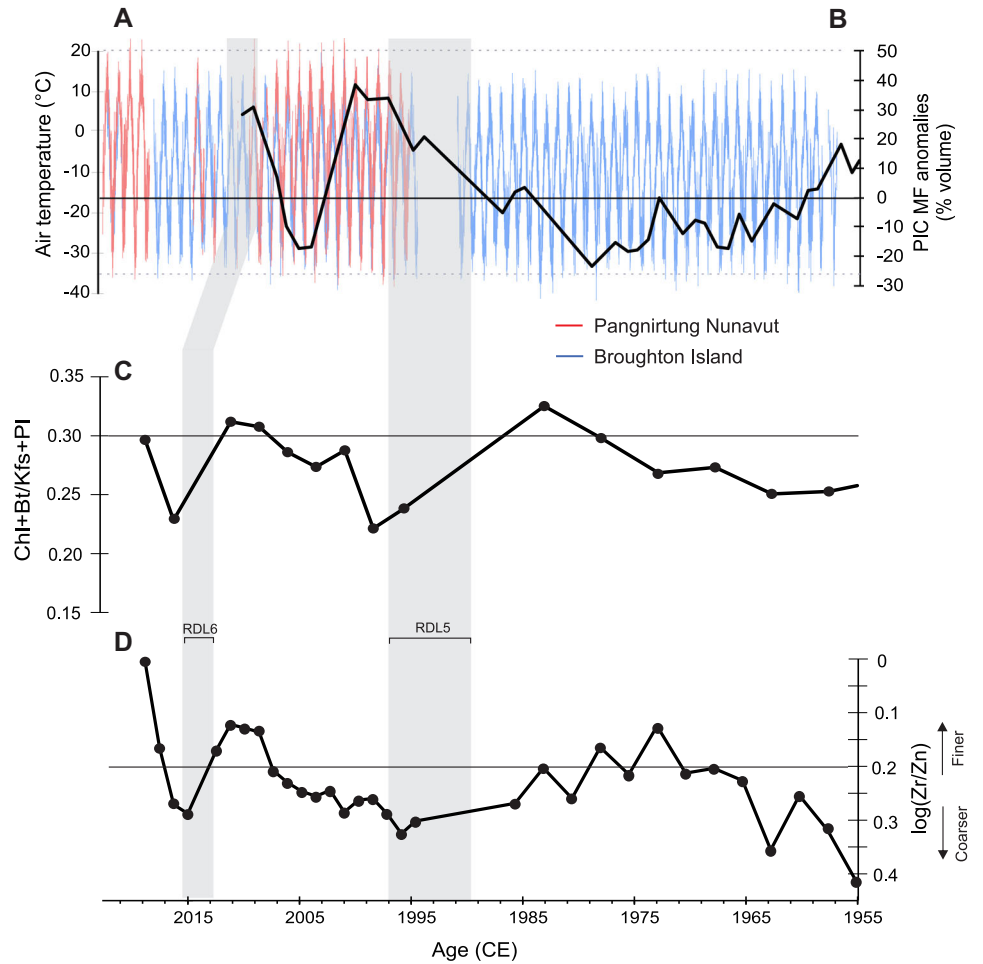
Depositional processes during the Late Holocene

The variations in the detrital proxies in the ice-proximal (12CS) and ice-distal (02CS) composite cores are used to explore the potential impacts of the Little Ice Age (LIA; ~1350–1850 CE; Jones & Mann, 2004) and modern warming (MW; late 1800s CE; Jones & Mann, 2004; Kaufman et al., 2009) on the sedimentary dynamics in these glacimarine environments.

Colder conditions associated with the LIA were regionally established on Baffin Island (e.g. Moore et al., 2001; Thomas & Briner, 2009; Kaufman et al., 2009; Miller et al., 2012). In core 12CS, the higher gravel-sized clast contents observed between ~1400 and ~1600 CE suggest a marked increase in the delivery of coarse-grained sediment by iceberg rafting at this time (Fig. 10D). The presence of laminated sediments and coarse ice-rafted clasts throughout the LIA interval (Unit 1 and the base of Unit 2) suggests that the sedimentary regime in Coronation Fjord was influenced by successive episodes of snowmelt runoff and turbid hyperpycnal meltwater plumes during spring/summer, as well as by increased iceberg calving activity of the Coronation Glacier. Previous Arctic paleoclimate studies (Kaufman et al., 2009; Thomas & Briner, 2009; Beaudoin et al., 2016; Lapointe et al., 2020) and climate model simulations (Crespin et al., 2009) provide evidence for short-term warming superimposed over general LIA cooling between ~1375 and ~1575 CE that was driven by the enhanced advection of warm air and Atlantic water to the Arctic (Kinnard et al., 2011; Miller et al., 2012). In this context, we argue that
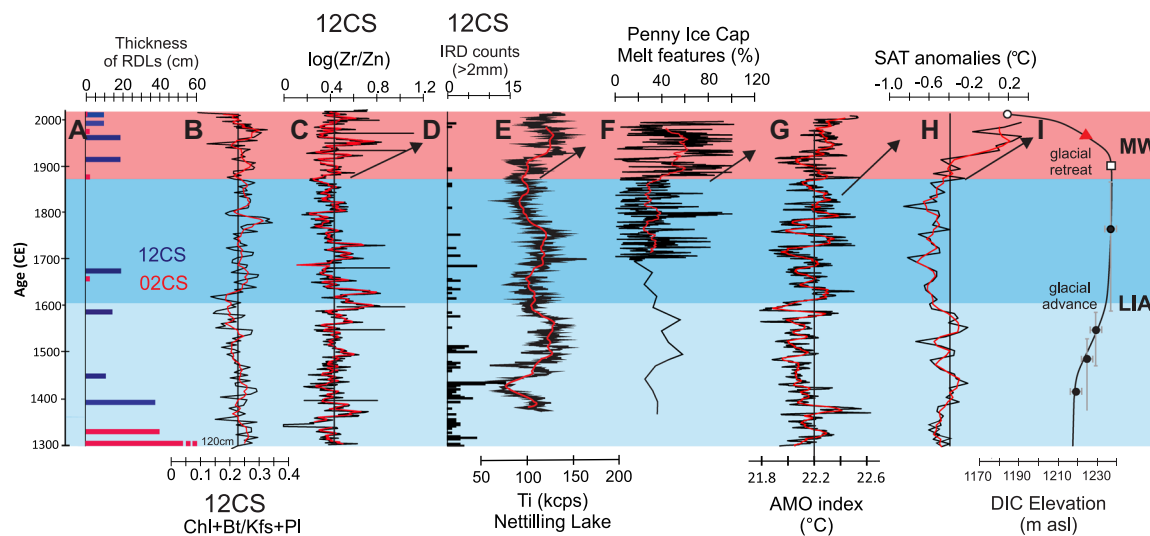
Figure 10. Comparison of detrital proxies used in this study for cores 12CS and 02CS during the Late Holocene with paleoenvironmental proxies. (A) Thickness of RDLs (blue bars: 12CS; red bars: 02CS); (B) Chl+Bt/Kfs+Pl; (C) log(Zr/Zn); (D) IRD count of core 12CS (>2 mm); (E) Ti (10^3 cps) measured in core sediment from Nettilling Lake (Beaudoin et al., 2016); (F) melt feature (MF) anomalies from the Penny Ice Cap (PIC; Fisher et al., 1998); (G) reconstructed Atlantic Multidecadal Oscillation (AMO) index (Lapointe et al., 2020); (H) surface air temperature (SAT) anomalies in the Arctic (Kaufman et al., 2009); and (I) inferred ice margin elevation of the Divide Ice Cap (DIC) located close to the Coronation Fjord (Pendleton et al., 2017). The position of the DIC margin was interpreted from radiocarbon ages of plants (black circles), aerial photography (triangle) and observed 2015 position (circle). The Neoglacial maximum DIC extent is also shown (square). asl = above sea level. The black vertical line represents the median of the data for each proxy. [Color figure can be viewed at wileyonlinelibrary.com]

Figure 11. Comparison of the (A) historical daily maximum air temperature data of Pangnirtung Nunavut and Broughton Island (source: https://climat.meteo.gc.ca) and (B) melt feature (MF) anomalies from the Penny Ice Cap (PIC; Zdanowicz et al., 2012), with (C) Chl+Bt/Kfs+Pl and (D) log(Zr/Zn) profiles from core 05BC (top of 02CS). The horizontal line represents the median of the data for each proxy. The log(Zr/Zn) scale was inverted for better comparison with the other proxies. Note that the difference in the timing between peaks of melt feature anomalies from the PIC and the sedimentary records reflects uncertainties in the individual chronology methods and/or a lag of the sediment response. [Color figure can be viewed at wileyonlinelibrary.com]

Figure 12. Schematic models of sedimentary processes and environmental conditions in Coronation Fjord during: (A) the LIA, with warmer episodes generating increased iceberg calving activity, increasing the concentration of IRD and turbidite deposits in an ice-proximal setting – successive episodes of high seasonal meltwater discharge resulted in outburst floods deposited in an ice-distal setting; and (B) MW, in which warmer conditions promoted the input of glacial meltwater outwash, sediment-laden transport and turbid hyperpycnal flow formation in ice-proximal and ice-distal settings. [Color figure can be viewed at wileyonlinelibrary.com]

the LIA promoted glacier growth into the fjord but that higher Arctic air temperatures together with extended melt seasons during this warm phase of the LIA promoted a substantial increase in calving activity in the Coronation Glacier (Fig. 12A). Conversely, the decrease in IRD content and $\overline{SS}$ values observed between 1750 and 1850 CE in core 12CS (Figs. 4A, D and 10F) support the idea that lower LIA temperatures established during this period promoted greater glacier growth in the region, an enhanced sea ice cover and a slowdown of the bottom current velocity in the fjord (Fig. 12A). A glaciological study performed in Divide Ice Cap (Pendleton et al., 2017), a small ice cap located close to Coronation Fjord (Fig. 2A), suggests that cold climatic conditions established before and during the LIA promoted episodic advances in this ice cap at ~1000, ~1200 and ~1500 CE, which led to the maximum Neoglacial dimensions ~1900 CE, in line with our interpretations. Although the exact marine glacier termini configuration of the Coronation Glacier during LIA is uncertain, we infer the position in Fig. 2B as close to the grounding line, which is in general agreement with observed changes in vegetation on the left side of the fjord (Davis, 1985; Pendleton et al., 2017). In Fig. 2B, it is possible to see that the ice front was at least ~2.4 km ahead of the current position of the glacier and did not advance to the 12CS core position.

Furthermore, the Chl+Bt/Kfs+Pl and log(Zr/Zn) profiles in core 12CS show a similar pattern of variations with those of the Ti record from Nettilling Lake (Beaudoin et al., 2016), melt feature anomalies from the PIC (Fisher et al., 1998), reconstructed Atlantic Multidecadal Oscillation (AMO) index values (Lapointe et al., 2020) and surface air temperature (SAT) anomalies in the Arctic (Kaufman et al., 2009) (Fig. 10). Indeed, high Chl+Bt and Zn contents and low IRD inputs recorded in core 12CS during the LIA correspond to a dominance of the negative AMO phase, lower Arctic SAT and reduced summer PIC melt rates (Fig. 10). This good correspondence suggests that at multidecadal to centennial timescales, the sedimentary dynamics in Coronation Fjord during the pre-industrial period may have been modulated by internal coupled atmosphere–ocean–ice interactions.

The higher sedimentation rates (~0.9 cm a^{-1} in core 12CS and 0.4 cm a^{-1} in core 02CS; Fig. 8) and the greatest variations in our detrital proxies are observed after ~1850 CE (Figs. 11 and 12), suggesting an increase in snowmelt runoff and glacial meltwater plumes from the eastern PIC margin, probably related to the influence of the modern warming trend (Kaufman et al., 2009; Zdanowicz et al., 2012). The increase in the coarse silt contents and log(Zr/Zn) ratios, together with the low Chl+Bt/Kfs+Pl ratios and IRD contents since ~1850 CE, suggests that glacial meltwater outwash (composed mainly of silt-sized particles) impact sedimentation in Coronation Fjord. Indeed, the landward retreat of marine-terminating glaciers promotes the formation of glacial outwash plains and deltas at the glacial front (Powell, 1981). In this setting, glacial meltwater streams can introduce a mixture of fine-grained sand and glacial flour silts over fan deltas and in more ice-distal marine locations (Powell, 1981; Dowdeswell et al., 2015; Stevenard et al., 2022). Similarly, during the winter season, rapid ice formation in shallow-water areas at the head of the fjord can foster the recurrent incorporation of proglacial outwash sediments into both sea ice via suspension freezing and anchor ice (e.g. Reimnitz et al., 1987) (Fig. 12B). Then, these sediments are entrained by surface currents in the fjord during the spring season. In this context, we hypothesize that the sedimentary regime in Coronation Fjord during the industrial period (1850 CE to present) was mainly driven by both an enhanced input of glacial meltwater outwash and the transport of sediment-laden sea ice through the fjord related to a landward retreat of the eastern PIC margin. In addition, the similar trend

observed between the Chl+Bt/Kfs+Pl and log(Zr/Zn) ratios from core 05BC with summer PIC melt rates (Fig. 11) supports the idea that increases in atmospheric temperatures observed since 1980 CE (linked to anthropogenically induced Arctic amplification; Kaufman et al., 2009) are an important factor driving the increase in summer ice melt rates of ice caps and glaciers on Baffin Island during the industrial period (e.g. Moore et al., 2001; Zdanowicz et al., 2012; Beaudoin et al., 2016; Cook et al., 2019). In addition, the most recent turbidite observed in core 02CS (RDL 6: 2013–2015 CE; Fig. 11C, D) may have been triggered by a marked increase in air temperature recorded for the region in 2009 (Fig. 11A). This also agrees with a decrease in the PIC mass balance for the period 2005–2014 (Schaffer et al., 2017). Thus, our results corroborate that the sedimentary dynamics of the Coronation Fjord show high fidelity to modern climate observations and represent a high-quality paleoclimate archive.

The occurrence of RDLs also correlates with the regional climatic variations (Fig. 10A). During the LIA, the thick RDLs in cores 12CS and 02CS (~20 to 120 cm thick) show a frequency of about one RDL per century, while the RDLs in the 20th century are thinner but more frequent (about RDLs per century and ~10 to 20 cm thick; Fig. 10A). These results suggest an increased frequency of RDLs during the MW compared to the LIA, probably related to increased summer ice melt rates of the eastern margin of the PIC. However, as RDLs have erosion/ transport potential and may lead to erosion of underlying RDLs (particularly RDL 1 and 2 in core 02CS), this interpretation needs to be taken with caution. Regardless, these results highlight the strong glaciological and hydrometeorological component in the triggering, intensity and frequency of the RDL deposits along Coronation Fjord.

Conclusions

Our multiproxy study on two sediment cores (12CS and 02CS) recovered along Coronation Fjord allowed us to trace the evolution of the sedimentary dynamics of the eastern PIC margin, as well as document glaciological processes and environmental conditions during the last 600 years. Overall, the results of this study yield the following generalizations and conclusions:

- The RDLs in the ice-proximal environment (core 12CS) were probably triggered by hyperpycnal flows of rock flour-laden meltwater (RDLs 1–3) and turbidity currents (RDLs 4–8). The recent RDLs in the ice-distal environment (core 02CS) were probably generated by meteorological outburst floods (RDLs 1 and 2) and by turbid hyperpycnal meltwater plumes (RDLs 3–6) sourced from Coronation, Maktak and North Pangnirtung Fjords. RDLs were more frequent during both the cold LIA and the warmer 19th–20th century periods and were probably the result of enhanced summer ice melt rates of the eastern PIC margin, respectively.
- The presence of laminated sediments and coarse ice-rafted clasts throughout the LIA period in core 12CS reveal that colder LIA conditions promoted glacier growth as well as successive episodes of turbid hyperpycnal meltwater plumes during spring/summer and increased iceberg calving activity in Coronation Fjord.
- The higher sedimentation rates (~0.9 cm a^{-1} in core 12CS and 0.4 cm a^{-1} in core 02CS), the increase in the coarse silt contents and the high frequency of RDLs observed since ~1850 CE are interpreted as indicating an accelerated retreat of the Coronation Glacier and enhanced summer ice melt rates from the eastern PIC margin due to 19th–20th century warming.
- Similar trends observed between our detrital proxies and summer melt features recorded from the PIC, AMO index

values and Arctic SAT anomalies suggest high connectivity between atmospheric and ocean temperature variations and the sedimentary dynamics of the Coronation Glacier during the last 600 years.

Supporting information

Additional supporting information can be found in the online version of this article.

Fig. S1. (a) D90. (b) ^{210}Pb excess profiles for core 05BC. (c) Application of a CFCS model to the event-free sedimentary profile of ^{210}Pb excess (without the thick graded beds, which are considered instantaneous deposits). (d) $^{239+240}$Pu profile (FF 1955: the radionuclide was introduced with atmospheric nuclear testing; NWT 1963: the abundance peaked at the height of testing in 1963). (e) Resulting age–depth model with 1σ uncertainties.

Fig. S2. Total ^{210}Pb, density, k_{LF} and D90 profiles for the first 130 cm of core 12TWC. The ^{210}Pb excess profile shows 'event horizons' with irregular ^{210}Pb and mineral compositions that are typical of periodic inputs of highly mobile sediment (e.g. Xu et al., 2015; Arias-Ortiz et al., 2018).

Fig. S3. (A) Illustration of ΔR and uncertainty calculation for samples with independently measured calendar ages (e.g. paleomagnetic ages). (B) ΔR over time obtained from paired ^{14}C and paleomagnetic ages of core 12PC using Marine20 marine radiocarbon age calibration curves on the program deltar (http://calib.org/deltar/). Horizontal errors represent the uncertainty of paleomagnetic ages, in 2σ; vertical errors (ΔR) are 1σ. Solid and dashed horizontal lines denote the median of ΔR from all samples, plus or minus one standard deviation.

Fig. S4. Core top correlations of core 12TWC with 12PC and cores 05BC and 02PC with the help of physical and chemical parameters to obtain composite depths of the 12CS and 02CS cores.

Fig. S5. Downcore mineralogical variations in cores 12CS (A) and 02CS (B). The vertical gray lines delineate the median values, and the red lines are five-point moving averages.

Fig. S6. (A, C) Sortable silt mean size (SSmean) vs percentage of sortable silt (SS%) for cores 12CS and 02CS. (B, D) SSmean and the running five-point correlation profiles for cores 12CS and 02CS. The gray areas indicate sections of the sortable silt record that do not pass the reliability test of a down-core correlation coefficient >0.5 between SSmean and SS% (McCave & Andrews, 2019a).

Fig. S7. Quartz (Qz) – chlorite+biotite (Chl+Bt) – K-feldspar+plagioclase (Kfs+Pl) ternary plot, including sediment samples of cores 12CS and 02CS. The mineralogical data of surface sediments from the Coronation, Maktak and Pangnirtung fjords are from Andrews et al. (2018) and Andrews (2019).

Fig. S8. Q7/4 diagram for the 12CS and 02CS cores. Five areas are distinguished (Debret et al., 2011): clayey deposits, organic-rich deposits (chlorophyll *a* and by-products), altered organic matter deposits, iron-rich deposits and carbonate deposits.

Conflict of interest—No conflicts of interest have been declared by the authors.

Author contributions—María-Emilia Rodríguez-Cuicas performed all analysis, wrote the original draft of the manuscript and made the figures. Jean-Carlos Montero-Serrano led the project, acquired the funds for core sampling and analysis, ran the statistical analyses on the qXRD and pXRF data, made the Bayesian age model, and acquired the radiocarbon dates. Guillaume St-Onge co-led the project, supervised the physical and paleomagnetic analysis of sediment cores, and acquired the radiocarbon dates. Alexandre Normandeau co-led the project, acquired the funds for core sampling and assisted with data interpretation. All authors contributed to reviewing and editing the manuscript.

Data availability statement

The data that support the findings of this study are openly available in https://doi.org/10.1594/PANGAEA.950888. All analytical data presented will be available electronically in the PANGAEA database (https://www.pangaea.de/).

Abbreviations. AMO, Atlantic Multidecadal Oscillation; AMS, accelerator mass spectrometry; BaIC, Barnes Ice Cap; BIC, Baffin Island Current; BI, broghton island; BT, Broughton Trough CAA, Canadian Arctic Archipelago; CCGS, Coastal Canadian Guard Ship; DIC, Divide Ice Cap; GL, grounding line; GOF, glacial outburst flood IC, Irminger Current; IRD, ice rafted debris; IRM, isothermal remanent magnetization; ISMER, Institue des sciences de la mer de Rimouski; k_{LF}, low field magnetic susceptibility; LIA, Little Ice Age; LS, lower sandur; MDF$_{NRM}$, median destructive field of the natural remanent magnetization; MSCL, multi-sensor core logger; MW, Modern Warming; NL, Nettilling Lake; NRM, natural remanent magnetization; PCA, principal component analysis; PIC, Penny Ice Cap; RDL, rapidly deposited layer; SAT, surface air temperature; US, upper sandur; SIRM, saturation isothermal remanent magnetization; SIS, Seafloor Information System; UQAR, Université du Québec à Rimouski; WGC, West Greenland Current; X-CT, X-ray computed tomography; XRD, X-ray diffraction; pXRF, portable X-ray fluorescence.

References

Adegbie, A.T., Schneider, R.R., Röhl, U. & Wefer, G. (2003) Glacial millennial-scale fluctuations in central African precipitation recorded in terrigenous sediment supply and freshwater signals offshore Cameroon. *Palaeogeography, Palaeoclimatology, Palaeoecology*, 197(3–4), 323–333. Available at: https://doi.org/10.1016/S0031-0182(03)00474-7

Aitchison, J. (1982) The statistical analysis of compositional data. *Journal of the Royal Statistical Society: Series B (Methodological)*, 44(2), 139–160.

Aksu, A.E. (1983) Holocene and Pleistocene dissolution cycles in deep-sea cores of Baffin Bay and Davis Strait: palaeoceano-graphic implications. *Marine Geology*, 53, 331–348.

Andrews, J.T. (2000) Icebergs and iceberg rafted detritus (IRD) in the North Atlantic: facts and assumptions. *Oceanography*, 100–108.

Andrews, J.T. (2019) Baffin Bay/Nares Strait surface (seafloor) sediment mineralogy: further investigations and methods to elucidate spatial variations in provenance. *Canadian Journal of Earth Sciences*, 56(8), 814–828.

Andrews, J.T., Klein, A.J., Jenner, K.A., Jennings, A.E. & Campbell, C. (2018) The variability of Baffin Bay seafloor sediment mineralogy: the identification of discrete glacial sediment sources and application to Late Quaternary downcore analysis. *Canadian Journal of Earth Sciences*, 55(6), 620–639.

Appleby, P.G. & Oldfieldz, F. (1983) The assessment of ^{210}Pb data from sites with varying sediment accumulation rates. *Hydrobiologia*, 103(1), 29–35.

Arias-Ortiz, A., Masqué, P., Garcia-Orellana, J., Serrano, O., Mazarrasa, I., Marbà, N. et al. (2018) Reviews and syntheses: 210Pb-derived sediment and carbon accumulation rates in vegetated coastal ecosystems – setting the record straight. *Biogeosciences*, 15(22), 6791–6818.

Azetsu-Scott, K., Clarke, A., Falkner, K., Hamilton, J., Jones, E.P., Lee, C. et al. (2010) Calcium carbonate saturation states in the waters of the Canadian Arctic Archipelago and the Labrador Sea. *Journal of Geophysical Research*, 115, C11021.

Beaudoin, A., Pienitz, R., Francus, P., Zdanowicz, C. & St-Onge, G. (2016) Palaeoenvironmental history of the last six centuries in the Nettilling Lake area (Baffin Island, Canada): a multi-proxy analysis. *The Holocene*, 26(11), 1835–1846.

Ben Meftah, M., De Serio, F., De Padova, D. & Mossa, M. (2020) Hydrodynamic structure with scour hole downstream of bed sills. *Water*, 12(1), 186.

Blaauw, M. & Christen, J.A. (2011) Flexible paleoclimate age–depth models using an autoregressive gamma process. *Bayesian Analysis*, 6, 457–474.

Blott, S.J. & Pye, K. (2001) GRADISTAT: a grain size distribution and statistics package for the analysis of unconsolidated sediments. *Earth Surface Processes and Landforms*, 26, 1237–1248.

Bouma, A.H. (1962) *Sedimentology of Some Flysch Deposits. A Graphic Approach to Facies Interpretation.* Amsterdam: Elsevier.

Briner, J.P., Davis, P.T. & Miller, G.H. (2009) Latest Pleistocene and Holocene glaciation of Baffin Island, Arctic Canada: key patterns and chronologies. *Quaternary Science Reviews*, 28, 2075–2087.

Briner, J.P., Michelutti, N., Francis, D.R., Miller, G.H., Axford, Y., Wooller, M.J. et al. (2006) A multi-proxy lacustrine record of Holocene climate change on northeastern Baffin Island, Arctic Canada. *Quaternary Research*, 65(3), 431–442.

Bruel, R. & Sabatier, P. (2020) serac: an R package for ShortlivEd RAdionuclide chronology of recent sediment cores. *Journal of Environmental Radioactivity*, 225, 106449. Available at: https://doi.org/10.1016/j.jenvrad.2020.106449

Casse, M., Montero-Serrano, J.-C. & St-Onge, G. (2017) Influence of the Laurentide Ice Sheet and relative sea-level changes on sediment dynamics in the Estuary and Gulf of St. Lawrence since the last deglaciation. *Boreas*, 46, 541–561.

Ciracì, E., Velicogna, I. & Swenson, S. (2020) Continuity of the mass loss of the world's glaciers and ice caps from the GRACE and GRACE Follow-On missions. *Geophysical Research Letters*, 47(9), e2019GL086926.

Clarke, D.B. & Upton, B.G.J. (1971) Tertiary basalts of Baffin Island: field relations and tectonic setting. *Canadian Journal of Earth Sciences*, 8(2), 248–258.

Constable, C., Korte, M. & Panovska, S. (2016) Persistent high paleosecular variation activity in southern hemisphere for at least 10 000 years. *Earth and Planetary Science Letters*, 453, 78–86.

Cook, A.J., Copland, L., Noël, B.P.Y., Stokes, C.R., Bentley, M.J., Sharp, M.J. et al. (2019) Atmospheric forcing of rapid marine-terminating glacier retreat in the Canadian Arctic Archipelago. *Science Advances*, 5, eaau8507. https://doi.org/10.1126/sciadv.aau8507

Corminboeuf, A., Montero-Serrano, J.-C. & St-Louis, R. (2021a) Spatial and temporal distributions of polycyclic aromatic hydrocarbons in sediments from the Canadian Arctic Archipelago. *Marine Pollution Bulletin*, 171, 112729. Available at: https://doi.org/10.1016/j.marpolbul.2021.112729

Corminboeuf, A., Montero-Serrano, J.-C., St-Louis, R. Dalpé, A. & Gélinas, Y. (2021b) Pre- and post-industrial levels of polycyclic aromatic hydrocarbons in sediments from the Estuary and Gulf of St. Lawrence (eastern Canada). *Marine Pollution Bulletin*, 113219. https://doi.org/10.1016/j.marpolbul.2021.113219

Cowan, E.A. & Powell, R.D. (1991) Ice-proximal sediment accumulation rates in a temperate glacial fjord, southeastern Alaska. In: Anderson, J.B. & Ashley, G.M. (Eds.) *Glacial marine sedimentation; Paleoclimatic significance: Boulder, Colorado,* Geological Society of America Special Paper 261.

Crespin, E., Goosse, H., Fichefet, T. & Mann, M.E. (2009) The 15th century Arctic warming in coupled model simulations with data assimilation. *Climate of the Past*, 5, 389–401.

Croudace, I.W. & Rothwell, R.G. (Eds.). (2015) Micro-XRF Studies of Sediment Cores: Applications of a non-destructive tool for the environmental sciences (Vol. 17). Springer.

Davis, P.T. (1985) Neoglacial moraines on Baffin Island. In: Andrews, J.T. (Ed.) *Quaternary environments: eastern Canadian Arctic, Baffin Bay and western Greenland.* London: Allen and Unwin. pp. 682–718.

de Vernal, A., Bilodeau, G., Hillaire-Marcel, C. & Kassou, N. (1992) Quantitative assessment of carbonate dissolution in marine sediments from foraminifer linings vs. shell ratios: Davis Strait, northwest North Atlantic. *Geology*, 20(6), 527–530.

Debret, M., Sebag, D., Desmet, M., Balsam, W., Copard, Y., Mourier, B. et al. (2011) Spectrocolorimetric interpretation of sedimentary dynamics: the new "Q7/4 diagram". *Earth-Science Reviews*, 109(1–2), 1–19. Available at: https://doi.org/10.1016/j.earscirev.2011.07.002

Deschamps, C.-E., Montero-Serrano, J.-C. & St-Onge, G. (2018) Sediment Provenance Changes in the Western Arctic Ocean in Response to Ice Rafting, Sea Level, and Oceanic Circulation Variations Since the Last Deglaciation. *Geochemistry, Geophysics, Geosystems*, 19, 2147–2165.

Dowdeswell, J.A., Hogan, K.A., Arnold, N.S., Mugford, R.I., Wells, M., Hirst, J.P.P. et al. (2015) Sediment-rich meltwater plumes and ice-proximal fans at the margins of modern and ancient tidewater glaciers: observations and modelling. *Sedimentology*, 62(6), 1665–1692.

Duboc, Q., St-Onge, G. & Lajeunesse, P. (2017) Sediment records of the influence of river damming on the dynamics of the Nelson and Churchill Rivers, western Hudson Bay, Canada, during the last centuries. *The Holocene*, 27(5), 712–725.

Dyke, A.S., Andrews, J.T. & Miller, G.H. (1982) Quaternary geology of Cumberland Peninsula, Baffin Island, District of Franklin, Commission géologique du Canada, Mémoires no. 403.

Eberl, D.D. (2003) User guide to RockJock—A program for determining quantitative mineralogy from X-ray diffraction data. *USGS Open File Report*, 40, 03–78

Emmer, A. (2017) Glacier retreat and glacial lake outburst floods (GLOFs). In Oxford Research Encyclopedia of Natural Hazard Science.

Fisher, D.A., Koerner, R.M., Bourgeois, J.C., Zielinski, G., Wake, C., Hammer, C.U. et al. (1998) Penny ice cap cores, Baffin Island, Canada, and the Wisconsinan Foxe Dome connection: two states of Hudson Bay ice cover. *Science*, 279(5351), 692–695.

Gamboa, A., Montero-Serrano, J.-C., St-Onge, G., Rochon, A. & Desiage, P.A. (2017) Mineralogical, geochemical, and magnetic signatures of surface sediments from the Canadian Beaufort Shelf and Amundsen Gulf (Canadian Arctic). *Geochemistry, Geophysics, Geosystems*, 18, 488–512.

Gardner, A.S., Moholdt, G., Wouters, B., Wolken, G.J., Burgess, D.O., Sharp, M.J. et al. (2011) Sharply increased mass loss from glaciers and ice caps in the Canadian Arctic Archipelago. *Nature*, 473, 357–360.

Gardner, A., Moholdt, G., Arendt, A., & Wouters, B. (2012) Accelerated contributions of Canada's Baffin and Bylot Island glaciers to sea level rise over the past half century. *The Cryosphere*, 6, 1103–1125.

Gilbert, R. (1982a) The Broughton Trough on the continental shelf of eastern Baffin Island, Northwest Territories. *Canadian Journal of Earth Sciences*, 19, 1599–1607.

Gilbert, R. (1982b) Contemporary Sedimentary Environments on Baffin Island, N.W.T., Canada: glaciomarine Processes in Fiords of Eastern Cumberland Peninsula. *Arctic and Alpine Research*, 14, 1–12.

Gilbert, R. (1983) Sedimentary processes of Canadian Arctic fjords. *Sedimentary geology*, 36(2–4), 147–175.

Gilbert, R. (1985) Quaternary glaciomarine sedimentation interpreted from seismic surveys of fiords on Baffin Island, NWT. *Arctic*, 38(4), 271–280.

Gilbert, R., Naldrett, D.L. & Horvath, V.V. (1990) Holocene sedimentary environment of Cambridge fiord, Baffin Island, northwest Territories. *Canadian Journal of Earth Sciences*, 27(2), 271–280.

Grobe, H. (1987) A simple method for the determination of ice-rafted debris in sediment cores. *Polarforschung*, 57(3), 123–126.

Harig, C. & Simons, F.J. (2016) Ice mass loss in Greenland, the Gulf of Alaska, and the Canadian Archipelago: seasonal cycles and decadal trends. *Geophysical Research Letters*, 43(7), 3150–3159.

Heaton, T.J., Köhler, P., Butzin, M., Bard, E., Reimer, R.W., Austin, W.E.N. et al. (2020) Marine20—the marine radiocarbon age calibration curve (0–55,000 cal BP). *Radiocarbon*, 62(4), 779–820.

Howe, J.A., Austin, W.E.N., Forwick, M., Paetzel, M., Harland, R. & Cage, A.G. (2010) Fjord systems and archives: a review. *Geological Society, London, Special Publications*, 344, 5–15.

Jackson, A., Jonkers, A.R.T. & Walker, M.R. (2000) Four centuries of geomagnetic secular variation from historical records. *Philosophical Transactions of the Royal Society of London. Series A: Mathematical, Physical and Engineering Sciences*, 358, 957–990.

Jackson, G.D. & Berman, R.G. (2000) Precambrian metamorphic and tectonic evolution of northern Baffin Island, Nunavut, Canada. *The Canadian Mineralogist*, 38(2), 399–421.

Jenner, K.A., Campbell, D.C. & Piper, D.J.W. (2018) Along-slope variations in sediment lithofacies and depositional processes since the Last Glacial Maximum on the northeast Baffin margin, Canada. *Marine Geology*, 405, 92–107.

Jones, P.D. & Mann, M.E. (2004) Climate over past millennia. *Reviews of Geophysics*, RG2002, 1–42.

Kassambara, A. & Mundt, F. (2020) Factoextra: Extract and Visualize the Results of Multivariate Data Analyses. R Package Version 1.0.7. [Available at: https://cran.r-project.org/web/packages/factoextra/]

Kaufman, D.S., Schneider, D.P., McKay, N.P., Ammann, C.M., Bradley, R.S., Briffa, K.R. et al. (2009) Recent warming reverses long-term Arctic cooling. *Science*, 325(5945), 1236–1239.

Ketterer, M.E., Watson, B.R., Matisoff, G. & Wilsont, C.G. (2002) Rapid dating of recent aquatic sediments using Pu activities and 240Pu/239Pu as determined by quadrupole inductively coupled plasma mass spectrometry. *Environmental Science & Technology*, 36(6), 1307–1311.

Ketterer, M.E., Hafer, K.M., Jones, V.J. & Appleby, P.G. (2004) Rapid dating of recent sediments in Loch Ness: inductively coupled plasma mass spectrometric measurements of global fallout Plutonium. *Science of the Total Environment*, 322, 221–229. Available at: https://doi.org/10.1016/j.scitotenv.2003.09.016

Kinnard, C., Zdanowicz, C.M., Fisher, D.A., Isaksson, E., de Vernal, A. & Thompson, L.G. (2011) Reconstructed changes in Arctic sea ice over the past 1,450 years. *Nature*, 479, 509–512.

Kirschvink, J.L. (1980) The least-squares line and plane and the analysis of palaeomagnetic data. *Geophysical Journal International*, 62, 699–718.

Korte, M. & Constable, C. (2011) Improving geomagnetic field reconstructions for 0–3 ka. *Physics of the Earth and Planetary Interiors*, 188(3—4), 247–259.

Lacourse, T. & Gajewski, K. (2020) Current practices in building and reporting age–depth models. *Quaternary Research*, 96, 28–38. Available at: https://doi.org/10.1017/qua.2020.47

Lapointe, F., Bradley, R.S., Francus, P., Balascio, N.L., Abbott, M.B., Stoner, J.S., et al. (2020). Annually resolved Atlantic sea surface temperature variability over the past 2,900 y. *Proceedings of the National Academy of Sciences*, 117(44), 27171–24178.

Lenaerts, J.T.M., van Angelen, J.H., van den Broeke, M.R., Gardner, A.S., Wouters, B. & van Meijgaard, E. (2013) Irreversible mass loss of Canadian Arctic Archipelago glaciers. *Geophysical Research Letters*, 40, 870–874.

Lévesque, Y., St-Onge, G., Lajeunesse, P., Desiage, P.A. & Brouard, E. (2020) Defining the maximum extent of the Laurentide Ice Sheet in Home Bay (eastern Arctic Canada) during the Last Glacial episode. *Boreas*, 49, 52–70.

Liu, D., Bertrand, S., Vandekerkhove, E. & Renson, V. (2021) Provenance of Baker River sediments (Chile, 48° S): Implications for the identification of flood deposits in fjord sediments. *Earth Surface Processes and Landforms*, 47(3), 1–13.

Mazaud, A. (2005) User-friendly software for vector analysis of the magnetization of long sediment cores. *Geochemistry, Geophysics, Geosystems*, 6(12), n/a.

McCave, I.N. & Andrews, J.T. (2019a) Distinguishing current effects in sediments delivered to the ocean by ice. I. Principles, methods and examples. *Quaternary Science Reviews*, 212, 92–107.

McCave, I.N. & Andrews, J.T. (2019b) Distinguishing current effects in sediments delivered to the ocean by ice. II. Glacial to Holocene changes in high latitude North Atlantic upper ocean flows. *Quaternary Science Reviews*, 223, 105902.

McCave, I.N., Manighetti, B. & Robinson, S.G. (1995) Sortable silt and fine sediment size/composition slicing: parameters for palaeocurrent speed and palaeoceanography. *Paleoceanography*, 10(3), 593–610.

McKenna-Neuman, C. & Gilbert, R. (1986) Aeolian processes and landforms in glaciofluvial environments of southeastern Baffin Island, NWT, Canada.

Miller, G.H., Geirsdóttir, Á., Zhong, Y., Larsen, D.J., Otto-Bliesner, B.L., Holland, M.M. et al. (2012) Abrupt onset of the Little Ice Age triggered by volcanism and sustained by sea-ice/ocean feedbacks. *Geophysical Research Letters*, 39(2), n/a.

Montero-Serrano, J.-C., Palarea-Albaladejo, J., Martín-Fernández, J.-A., Martínez-Santana, M. & Gutiérrez-Martín, J.V. (2010) Sedimentary chemofacies characterization by means of multivariate analysis. *Sedimentary Geology*, 228, 218–228. Available at: https://doi.org/10.1016/j.sedgeo.2010.04.013

Montero-Serrano, J.-C., Brossard, J. & Corminboeuf, A. (2018) Collecting sedimentary sequences for paleoclimate, paleoceanographic and environmental studies in the eastern Canadian Arctic Archipelago and Baffin Bay. ArcticNet Leg 3 Cruise Report - CCGS Amundsen expedition (16 August to 9 September). ArcticNet p. 14.

Moore, J.J., Hughen, K.A., Miller, G.H. & Overpeck, J.T. (2001) Little Ice Age recorded in summer temperature reconstruction from vared sediments of Donard Lake, Baffin Island, Canada. *Journal of Paleolimnology*, 25(4), 503–517.

Mulder, T. & Syvitski, J.P.M. (1995) Turbidity currents generated at river mouths during exceptional discharges to the world oceans. *The Journal of Geology*, 103, 285–299.

Mulder, T., Migeon, S., Savoye, B. & Faugères, J. C. (2001) Inversely graded turbidite sequences in the deep Mediterranean: a record of deposits from flood-generated turbidity currents? *Geo-marine letters*, 21, 86–93.

Mulder, T., Syvitski, J.P.M., Migeon, S., Faugères, J.C. & Savoye, B. (2003) Marine hyperpycnal flows: initiation, behavior and related deposits. A review. *Marine and Petroleum Geology*, 20(6-8), 861–882.

Münchow, A., Falkner, K.K. & Melling, H. (2015) Baffin Island and west Greenland current systems in northern Baffin bay. *Progress in Oceanography*, 132, 305–317.

Narancic, B., Saulnier-Talbot, É., Meyer, H. & Pienitz, R. (2021) A 5000-year paleoclimate record from Nettilling Lake (Baffin Island) based on diatom assemblages and oxygen isotope composition. *Journal of Quaternary Science*, 37(5), 959–966.

Noël, B., van de Berg, W.J., Lhermitte, S., Wouters, B., Schaffer, N. & van den Broeke, M.R. (2018) Six Decades of Glacial Mass Loss in the Canadian Arctic Archipelago. *Journal of Geophysical Research: Earth Surface*, 123, 1430–1449.

Normandeau, A., Broom, L.M., Carson, T. & Trottier, A.-P. (2019) CCGS Amundsen 2019804 expedition: marine geohazards and sediment transport processes in Baffin Bay, Nunavut; Geological Survey of Canada, Open File 8649, 25 p. https://doi.org/10.4095/321054

Normandeau, A., MacKillop, K., Macquarrie, M., Richards, C., Bourgault, D., Campbell, D.C. et al. (2021) Submarine landslides triggered by iceberg collision with the seafloor. *Nature Geoscience*, 14(8), 599–605.

O Cofaigh, C., Dowdeswell, J.A., Jennings, A.E., Hogan, K.A., Kilfeather, A., Hiemstra, J.F. et al. (2013) An extensive and dynamic ice sheet on the West Greenland shelf during the last glacial cycle. *Geology*, 41(2), 219–222.

Oerlemans, J. (2005) Extracting a climate signal from 169 glacier records. *Science*, 308, 675–677.

Palarea-Albaladejo, J. & Martín-Fernández, J.A. (2015) zCompositions — R package for multivariate imputation of left-censored data under a compositional approach. *Chemometrics and Intelligent Laboratory Systems*, 143, 85–96.

Pendleton, S.L., Miller, G.H., Anderson, R.A., Crump, S.E., Zhong, Y., Jahn, A. et al. (2017) Episodic Neoglacial expansion and rapid 20th century retreat of a small ice cap on Baffin Island, Arctic Canada, and modeled temperature change. *Climate of the Past*, 13, 1527–1537.

Philippe, É.G.H., Valet, J.P., St-Onge, G. & Thevarasan, A. (2018) Are paleomagnetic records from U-channels appropriate for studies of reversals and excursions? *Geochemistry, Geophysics, Geosystems*, 19, 4130–4142.

Philippe, É.G.H., Valet, J.P., St-Onge, G. & Egli, R. (2022) Impact of turbulence on magnetic alignment in sediments. *Frontiers in Earth Science*, 10, 1079229.

Pope, E.L., Normandeau, A., Ó Cofaigh, C., Stokes, C.R. & Talling, P.J. (2019) Controls on the formation of turbidity current channels associated with marine-terminating glaciers and ice sheets. *Marine Geology*, 415, 105951.

Powell, R.D. (1981) A model for sedimentation by tidewater glaciers: Annals of Glaciology, v. 2, p. 129–134.

Powell, R.D. (1985) Iceberg calving and its influence on ice-proximal, subaqueous glacigenic lithofacies, in Abstracts of the 14th Arctic Workshop on Arctic Land- Sea Interaction: Canada, Bedford Institute of Oceanography, p. 101–103.

R Core Team. (2021) R: A language and environment for statistical computing. R Foundation for Statistical Computing, Vienna, Austria. Available at: https://www.R-project.org/

Radić, V. & Hock, R. (2010) Regional and global volumes of glaciers derived from statistical upscaling of glacier inventory data. *Journal of Geophysical Research*, 115, F01010.

Reimer, R.W. & Reimer, P.J. (2017) An online application for ΔR calculation. *Radiocarbon*, 59(5), 1623–1627.

Reimnitz, E., Kempema, E.W. & Barnes, P.W. (1987) Anchor ice, seabed freezing, and sediment dynamics in shallow Arctic seas. *Journal of Geophysical Research*, 92, 14671–14678.

Reyss, J.-L., Schmidt, S., Legeleux, F. & Bonté, P. (1995) Large, low background well-type detectors for measurements of environmental radioactivity. *Nuclear Instruments and Methods in Physics Research Section A: Accelerators, Spectrometers, Detectors and Associated Equipment*, 357, 391–397. Available at: https://doi.org/10.1016/0168-9002(95)00021-6

Russell, N., Cook, G.T., Ascough, P.L., Scott, E.M. & Dugmore, A.J. (2011) Examining the inherent variability in ΔR: new methods of presenting ΔR values and implications for MRE studies. *Radiocarbon*, 53, 277–288. Available at: https://doi.org/10.1017/S003382220005654X

Schaffer, N., Copland, L. & Zdanowicz, C. (2017) Ice velocity changes on Penny Ice Cap, Baffin Island, since the 1950s. *Journal of Glaciology*, 63, 716–730.

Schatz, E.R., Mángano, M.G., Aitken, A.E. & Buatois, L.A. (2013) Response of benthos to stress factors in Holocene Arctic fjord settings: maktak, Coronation, and North Pangnirtung Fjords, Baffin Island, Canada. *Palaeogeography, Palaeoclimatology, Palaeoecology*, 386, 652–668.

Schmidt, M., Leipe, C., Becker, F., Goslar, T., Hoelzmann, P., Mingram, J. et al. (2019) A multi-proxy palaeolimnological record of the last 16,600 years from coastal Lake Kushu in northern Japan. *Palaeogeography, Palaeoclimatology, Palaeoecology*, 514, 613–626. Available at: https://doi.org/10.1016/j.palaeo.2018.11.010

Shaw, J. (1987) Glacial sedimentary processes and environmental reconstruction based on lithofacies. *Sedimentology*, 34, 103–116.

Stevenard, N., Montero-Serrano, J.-C., Eynaud, F., St-Onge, G., Zaragosi, S. & Copland, L. (2022) Lateglacial and Holocene sedimentary dynamics in northwestern Baffin Bay as recorded in sediment cores from Cape Norton Shaw Inlet (Nunavut, Canada). *Boreas*, 51, 532–552. Available at: https://doi.org/10.1111/bor.12575

Stoner, J.S. & St-Onge, G. (2007) Chapter Three Magnetic Stratigraphy in Paleoceanography: Reversals, Excursions, Paleointensity, and Secular Variation. In: Hillaire–Marcel, C. & De, A. (Eds.) *Vernal. Developments in Marine Geology*. Elsevier. pp. 99–138.

St-Onge, M.R., Van Gool, J.A.M., Garde, A.A. & Scott, D.J. (2009) Correlation of Archaean and Palaeoproterozoic units between northeastern Canada and western Greenland: constraining the pre-collisional upper plate accretionary history of the Trans-Hudson orogen. *Geological Society, London, Special Publications*, 318(1), 193–235.

St-Onge, G., Mulder, T., Francus, P. & Long, B. (2007) Chapter Two Continuous Physical Properties of Cored Marine Sediments. In: Hillaire–Marcel, C. & De Vernal, A. (Eds.) *Developments in Marine Geology*. Elsevier. pp. 63–98.

St-Onge, G., Mulder, T., Piper, D.J.W., Hillaire-Marcel, C. & Stoner, J.S. (2004) Earthquake and flood-induced turbidites in the Saguenay Fjord (Québec): a Holocene paleoseismicity record. *Quaternary Science Reviews*, 23(3-4), 283–294.

Syvitski, J.P.M. (1989) On the deposition of sediment within glacier-influenced fjords: oceanographic controls. *Marine Geology*, 85, 301–329.

Syvitksi, J. & Normandeau, A. (2023) Sediment redistribution processes in Baffin Island Fjords. *Marine Geology*, 458, 107024.

Syvitski, J.P.M. & Schafer, C.T. (1985) Sedimentology of arctic fiords experiment (SAFE): project introduction. *Arctic*, 38, 264–270.

Syvitski, J.P. & Shaw, J. (1995) Sedimentology and geomorphology of fjords, In: *Developments in sedimentology*, 53. Elsevier. pp. 113–178.

Syvitski, J.P. & Piper, D.J. (1990) Baffin Island Fiords. In: Keen, M.J. & Williams, G.L. (Ed.) *Chapter 10 of Geology of the Continental Margin of Eastern Canada*, no. 2. Geological Survey of Canada, Geology of Canada. pp. 563–566.

Syvitski, J., Andrews, J.T., Schafer, C.T. & Stravers, J.A. (2022) Sediment fill of Baffin Island fjords: architecture and rates. *Quaternary Science Reviews*, 284, 107474.

Tang, C.C.L., Ross, C.K., Yao, T., Petrie, B., DeTracey, B.M. & Dunlap, E. (2004) The circulation, water masses and sea-ice of Baffin Bay. *Progress in Oceanography*, 63, 183–228.

Tanty, C., Valet, J.P., Carlut, J., Bassinot, F. & Zaragosi, S. (2016) Acquisition of detrital magnetization in four turbidites. *Geochemistry, Geophysics, Geosystems*, 17(8), 3207–3223.

Telford, R., Heegaard, E. & Birks, H. (2004) All age–depth models are wrong: but how badly? *Quaternary science Reviews*, 23, 1–5. Available at: https://doi.org/10.1016/j.quascirev.2003.11.003

Thomas, E.K. & Briner, J.P. (2009) Climate of the past millennium inferred from varved proglacial lake sediments on northeast Baffin Island, Arctic Canada. *Journal of Paleolimnology*, 41(1), 209–224.

Thomas, E.K., Briner, J.P., Axford, Y., Francis, D.R., Miller, G.H. & Walker, I.R. (2011) A 2000-yr-long multi-proxy lacustrine record from eastern Baffin Island, Arctic Canada reveals first millennium AD cold period. *Quaternary Research*, 75(3), 491–500.

Trachsel, M. & Telford, R.J. (2017) All age–depth models are wrong, but are getting better. *The Holocene*, 27, 860–869. Available at: https://doi.org/10.1177/0959683616675939

Van den Boogaart, K.G. & Tolosana-Delgado, R. (2008) "Compositions": a unified R package to analyze compositional data. *Computers & Geosciences*, 34(4), 320–338.

Van Wychen, W., Copland, L., Burgess, D.O., Gray, L. & Schaffer, N. (2015) Glacier velocities and dynamic discharge from the Ice masses of Baffin Island and Bylot Island, Nunavut, Canada. *Canadian Journal of Earth Sciences*, 52, 980–989.

Vandekerkhove, E., Bertrand, S., Torrejón, F., Kylander, M.E., Reid, B. & Saunders, K.M. (2021) Signature of modern glacial lake outburst floods in fjord sediments (Baker River, southern Chile). *Sedimentology*, 68(6), 2798–2819.

von Eynatten, H., Barcelo-Vidal, C. & Pawlowsky-Glahn, V. (2003) Composition and Discrimination of sandstones: a statistical evaluation of different analytical methods. *Journal of Sedimentary Research*, 73, 47–57.

von Eynatten, H., Tolosana-Delgado, R. & Karius, V. (2012) Sediment generation in modern glacial settings: grain-size and source-rock control on sediment composition. *Sedimentary Geology*, 280, 80–92.

Weeks, R., Laj, C., Endignoux, L., Fuller, M., Roberts, A., Manganne, R. et al. (1993) Improvements in long-core measurement techniques: applications in palaeomagnetism and palaeoceanography. *Geophysical Journal International*, 114(3), 651–662.

Weltje, G.J. & Tjallingii, R. (2008) Calibration of XRF core scanners for quantitative geochemical logging of sediment cores: theory and application. *Earth and Planetary Science Letters*, 274(3–4), 423–438.

Wu, L., Wilson, D.J., Wang, R., Yin, X., Chen, Z., Xiao, W. et al. (2020) Evaluating Zr/Rb ratio from XRF scanning as an indicator of Grain-Size variations of glaciomarine sediments in the Southern Ocean. *Geochemistry, Geophysics, Geosystems*, 21, Available at: https://doi.org/10.1029/2020GC009350. e2020GC009350

Xu, B., Bianchi, T.S., Allison, M.A., Dimova, N.T., Wang, H., Zhang, L. et al. (2015) Using multi-radiotracer techniques to better understand sedimentary dynamics of reworked muds in the Changjiang River estuary and inner shelf of East China Sea. *Marine Geology*, 370, 76–86.

Zdanowicz, C., Smetny-Sowa, A., Fisher, D., Schaffer, N., Copland, L., Eley, J. et al. (2012) Summer melt rates on Penny Ice Cap, Baffin Island: past and recent trends and implications for regional climate. *Journal of Geophysical Research: Earth Surface*, 117(F2), F02006. https://doi.org/10.1029/2011JF002248